Giant spin Nernst effect in a two-dimensional antiferromagnet due to magnetoelastic coupling-induced gaps and interband transitions between magnon-like bands

D.-Q. To,[1] C. Y. Ameyaw,[1] A. Suresh,[2] S. Bhatt,[2] M. J. H. Ku,[1,2] M. B. Jungfleisch,[2] J. Q. Xiao,[2] J. M. O. Zide,[1] B. K. Nikolić,[2,*] and M. F. Doty[1,†]

[1] *Department of Materials Science and Engineering, University of Delaware, Newark, DE 19716, USA*

[2] *Department of Physics and Astronomy, University of Delaware, Newark, DE 19716, USA*

(Dated: May 17, 2023)

We analyze theoretically the origin of the spin Nernst and thermal Hall effects in $FePS_3$ as a realization of two-dimensional antiferromagnet (2D AFM). We find that a strong magnetoelastic coupling, hybridizing magnetic excitation (magnon) and elastic excitation (phonon), combined with time-reversal-symmetry-breaking, results in a Berry curvature hotspots in the region of anticrossing between the two distinct hybridized bands. Furthermore, large spin Berry curvature emerges due to *interband transitions between two magnon-like bands*, where a small energy gap is induced by magnetoelastic coupling between such bands that are *energetically distant* from anticrossing of hybridized bands. These nonzero Berry curvatures generate topological transverse transport (i.e., the thermal Hall effect) of hybrid excitations, dubbed magnon-polaron, as well as of spin (i.e., the spin Nernst effect) carried by them, in response to applied longitudinal temperature gradient. We investigate the dependence of the spin Nernst and thermal Hall conductivities on the applied magnetic field and temperature, unveiling very large spin Nernst conductivity *even* at zero magnetic field. Our results suggest $FePS_3$ AFM, which is already available in 2D form experimentally, as a promising platform to explore the topological transport of the magnon-polaron quasiparticles at THz frequencies.

I. INTRODUCTION

Two-dimensional (2D) antiferromagnets (AFMs [1] are attracting growing attention due to their potential application as material platforms for spintronics, spin-orbitronics, and spin-caloritronics [2–10]. Because the strong exchange interaction between their localized spins results in intrinsic THz frequency dynamics, AFMs are particularly promising for the development of devices with high operating speeds. For example, magnon in a 2D AFM can be employed to store and transfer THz frequency information without Joule heating due to the absence of a charge current or a stray field. Such materials can also provide efficient spin-transport channels in spintronic devices with low energy consumption [11–16]. Despite these advantages, the use of magnons in 2D AFMs as a part of realistic devices is severely limited by the lack of efficient ways to generate and manipulate magnon excitations. The hybridization of magnons and phonons may provide a path toward coherent control of magnons in 2D AFM material via a manipulation of the hybridized states [17–21]. For instance, it has been shown that one can electrically generate magnon spin current through the interaction between magnon and phonon [22, 23]. Conversely, it has also been shown that the dynamics of a phonon can be controlled via its interaction with a magnon [24–26].

Magnons and phonons are the collective and charge-neutral excitations of localized spins and lattice vibrations, respectively. They behave as bosonic quasiparticles, obeying the Bose-Einstein distribution function at finite temperature with zero chemical potential in equilibrium due to their non-conserved number. Strong coupling between a magnon and a phonon results in a hybridized state that includes both spin and lattice collective excitations in a single coherent mode [28–31]. As a result, a new type of quasiparticle, dubbed magnon-polaron [32, 33], is formed. The intriguing and non-trivial emergent properties of magnon-polarons provide a possible foundation for novel devices with unique optical and electrical functionalities [34–40]. In particular, the hybridization of magnons and phonons to create a magnon-polaron can generate a finite Berry and spin (generalized) Berry curvatures concentrated around anticrossing regions [28–31] of the magnon and phonon bands. These Berry curvatures then lead to nontrivial topological transverse transport—the magnon thermal Hall effect (THE) and magnon spin Nernst effect (SNE)—which have attracted a lot of attention [27–31, 33, 41–48]. In particular, recent studied have demonstrated [32, 49–52] possibly strong magnon-phonon coupling $FePS_3$ as the realization of 2D AFM. This, together with experimentally accessible 2D form of this material, makes $FePS_3$ a great candidate for investigation of magnon THE and SHE.

Let us recall that the magnon THE [43] refers to a phenomenon that occurs when a temperature gradient applied to a magnetic material generates transverse thermal transport of magnons, perpendicular to both the temperature gradient and magnetization. The magnon SNE [27], as an analogy of the electronic spin Hall effect (SHE) [53, 54] where electrons of opposite spin travel in opposite directions transverse to applied un-

* bnikolic@udel.edu
† doty@udel.edu

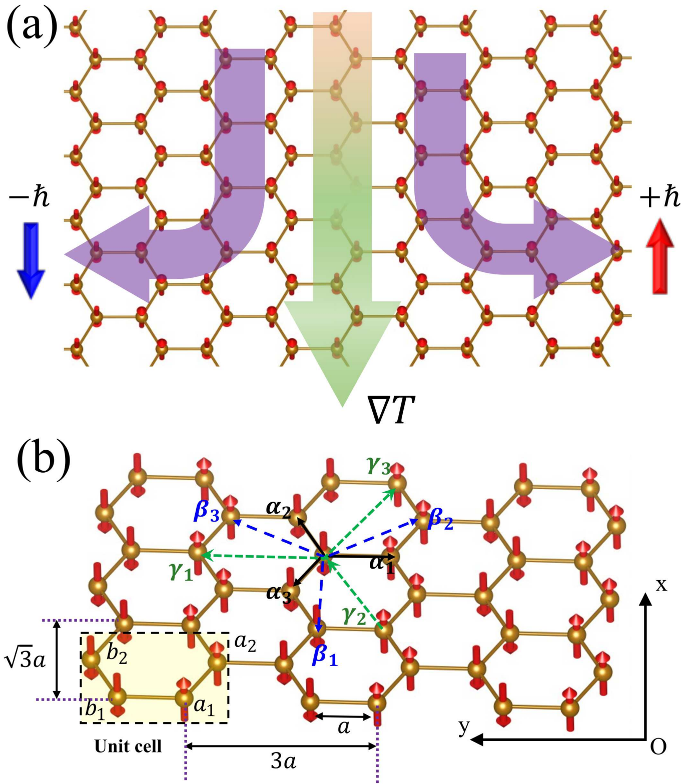

FIG. 1. (a) Schematic view of the magnon SNE in a 2D AFM where transverse flow of magnons carrying opposite out-of-the plane spins ($\pm\,\hbar$) is induced by temperature gradient ∇T along the longitudinal direction [27]. (b) The quasi-2D lattice of $FePS_3$ formed by Fe atoms. The arrows indicate the direction of the its localized spins within zigzag AFM phase considered in our study. Here α_i, β_i and γ_i $(i=1,2,3)$ are the vectors joining the first, second, and third-nearest neighbors, respectively. A unit cell contains four Fe atoms forming a rectangularly-shaped BZ with periodicity in real space that is $\sqrt{3}a$ or $3a$ long in the x- or y-directions (where a is the lattice constant), respectively.

polarized charge current, involves the flow of magnons instead of electrons carrying opposite spin flow in opposite directions perpendicular to the temperature gradient [Fig. 1(a)]. The magnon SNE is made possible by the existence of two magnon species within AFM carrying opposite spin polarization [27]. Recent studies have shown that the magnon SNE effect can be observed in: collinear antiferromagnets [27, 41, 55] on a honeycomb lattice, where the Dzyaloshinskii-Moriya interaction (DMI) acting [56] on magnons plays an analogous role as spin-orbit coupling (SOC) plays [53, 54] for electrons in the SHE; noncollinear antiferromagnets [47, 57], even without any SOC responsible for DMI, and in zero applied magnetic field; as well as in collinear antiferromagnets [29–31] or ferrimagnets [28] with magnetoelastic coupling hybridizing magnon and phonon quasiparticle bands whose anticrossing regions are putatively crucial [28] to obtain nonzero Berry and spin Berry curvature driving [see Sec. II B] transverse transport in THE and SNE, respectively.

In contrast, our study highlights a mechanism [31] where a significant spin Berry curvature can be induced in an energy window of magnon-like bands that is *energetically distant* [for example the 1st and 2nd band in Fig. 2(a)] from the magnon-phonon hybridized bands and their anticrossing within a collinear AFM. The magnon-like bands posses a small phonon character [Fig. 2(a)] over the entire Brillouin zone (BZ), which causes opening of slight band gaps between them [Fig. S2(b) in SM [58]]. These band gaps are actually *smaller* than anticrossing gap between magnon-like and phonon-like bands [Fig. S2(b) in SM [58]]. The *smallness* of band gaps between magnon-like bands [Figs. S2(b) and S3(b) in SM [58]] and phonon-mediated interband transitions [31] between them lead to significant spin Berry curvature (Fig. 5) and, thereby, the possibility of a giant SNE in $FePS_3$ collinear AFM.

The paper is organized as follows. In Sec. II we introduce an effective Hamiltonian to capture the magnon-phonon hybridization within 2D AFMs belonging to the MPX_3 (M = Fe, Mn, Co, Ni; X = S, Se) family hosting localized spins and their magnetic moments in a zigzag phase. The same Section also reviews the theoretical framework of linear-response theory that can be used to investigate the transverse transport of magnon-polaron quasiparticles. In Sec. III we discuss thus generated SNE and THE for $FePS_3$, including the dependence of the thermal Hall and spin Nernst conductivities on the applied magnetic field and temperature. We conclude in Sec. IV.

II. MODELS AND METHODS

A. 2D AFM Hamiltonian describing magnons, phonons and their magnetoelastic coupling

The MPX_3 (X = Fe, Mn, Co, Ni; X = S, Se) family of materials are van der Waals magnets [1] forming layered structures that are weakly bound by van der Waals forces and possess a stable magnetic order even in the monolayer limit [59, 60] because of a huge single ion anisotropy energy [33, 49, 61–64]. In particular, Fig. 1 shows the layered structure of $FePS_3$ that is established solely by the Fe atoms. Within each layer, the Fe atoms arrange in a honeycomb-like lattice structure with "columns" of spins having opposite spin moments. We consider the $FePS_3$ magnetic structure in the so-called zigzag AFM phase in which a unit cell contains two pairs of equivalent atoms (i.e., having the same spin direction) that are labelled as a_i and b_i $(i=1,2)$, respectively. Due to the small value of the interlayer exchange interaction relative to the intralayer exchange interaction, these AFMs are, to a very good approximation, quasi-two dimensional magnets even in the bulk [61, 65–69]. The magnon-phonon hybridization in $FePS_3$ can, therefore, be investigating by focusing on quasi-2D honeycomb structure of Fe atoms

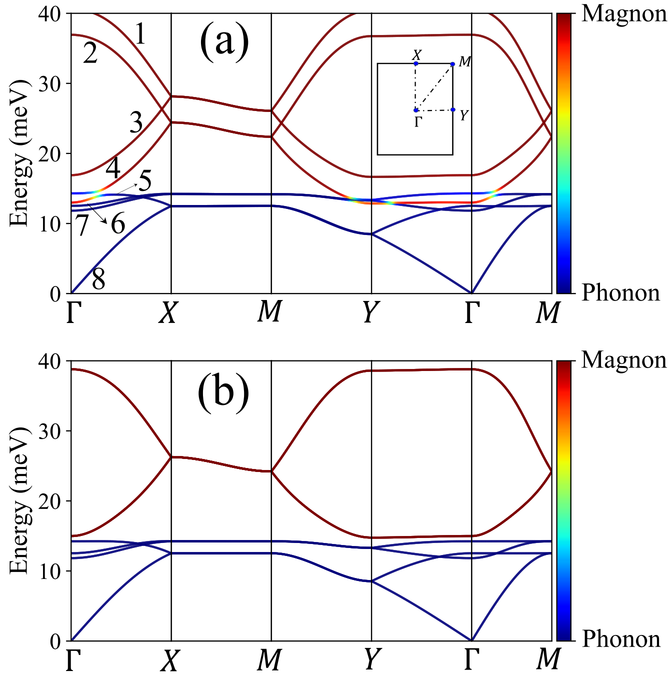

FIG. 2. (a) The hybridized magnon-phonon band structure of $FePS_3$ [Fig. 1], along Γ-X-M-Y-Γ-M high symmetry path in the BZ marked in the inset, calculated for an applied magnetic field of $B_z = 30$ T. The color scale bar encodes whether the bands have magnon-like, phonon-like, or mixed character. The bands are labelled 1–8 from the highest to the lowest energy. (b) The counterpart of panel (a), but in the absence of magnetoelastic coupling [$H_m = 0$ in Eq. (4)] and for zero applied magnetic field [$B_z = 0$ in Eq. (2)]. This means that red lines denote purely magnon bands and blue lines denote purely phonon bands of $FePS_3$, without any hybridization between them being present.

whose Hamiltonian can be written as

$$H = H_m + H_p + H_{mp}. \tag{1}$$

Here H_m is the Hamiltonian of localized spins whose low-energy excited states are magnons [14]; H_p is the phonon Hamiltonian; and H_{mp} is the term describing magnetoelastic coupling and thereby induced hybridization of magnons and phonons. The term H_m is the anisotropic Heisenberg model [61, 65–67, 70]:

$$H_m = \sum_{i,j} J_{ij} \boldsymbol{S}_i \boldsymbol{S}_j + \Delta \sum_i (S_i^z)^2 + g\mu_B B_z \sum_i S_i^z \tag{2}$$

where $\boldsymbol{S}_i = (S_i^x, S_i^y, S_i^z)$ is the operator of total spin localized at a site i of the lattice; J_{ij} is the exchange coupling between localized spins at sites i and j; Δ is the easy-axis anisotropy energy; the Zeeman (third on the right) term takes into account coupling to the applied magnetic field B_z pointing along the z-axis which is perpendicular to the plane in Fig. 1; g is the Landé g-factor; and μ_B is the Bohr magneton. The sum $\sum_{ij}$ runs over all atom pairs in the lattice up to the third-nearest neighbor.

We take into account the magnetoelastic coupling by assuming that it acts only between magnons and out-of-plane phonons. Such assumption is particularly relevant for $FePS_3$ 2D AFM, where out-of-plane phonon modes are closely aligned with the magnon modes in terms of energy and have been observed to hybridize with them under an applied magnetic field [49]. Therefore, we focus only on the z-component of the lattice vibrations, so that describing them with a simple harmonic oscillator model yields the following effective phonon Hamiltonian [45, 71]

$$H_p = \sum_i \frac{(p_i^z)^2}{2M} + \frac{1}{2} \sum_{ij} u_i^z \Phi_{i,j}^z u_j^z. \tag{3}$$

Here p_i^z and u_i^z are the operators of out-of-plane momentum and displacement of the atom at site i of the lattice, respectively; Φ^z is a spring constant matrix; and M is the mass of the atom. Finally, for the magnetoelastic coupling, which generates hybridization of magnon and phonon bands [Fig. 2(a)], we adopt Hamiltonian derived by Kittel [72] to linear order in the magnon amplitude, and adapted [49, 73] to magnons coupled to out-of-plane phonons in $FePS_3$

$$H_{mp} = -\xi \sum_i \left[\epsilon_i^{yz} \left(S_i^x S_i^z + S_i^z S_i^x\right) + \epsilon_i^{xz} \left(S_i^y S_i^z + S_i^z S_i^y\right)\right], \tag{4}$$

where ξ is the coupling strength and ϵ_i^{xz} and ϵ_i^{yz} are strain functions at the i site computed by averaging over the strain from nearest-neighboring ions

$$\epsilon_i^{\alpha\beta} = \frac{1}{N} \sum_j \epsilon_{ij}^{\alpha\beta}. \tag{5}$$

The two-ion strain tensor in the small displacement approximation is given by [73, 74]

$$\epsilon_{ij}^{\alpha\beta} = \frac{1}{2} \left[\left(r_i^\alpha - r_j^\alpha\right)\left(u_i^\beta - u_j^\beta\right) + \left(r_i^\beta - r_j^\beta\right)\left(u_i^\alpha - u_j^\alpha\right)\right], \tag{6}$$

where r_i^α and u_i^α are the α-component of the location vector in equilibrium and the displacement of the atom from equilibrium, respectively, for site i of the lattice.

The transformation of Eq. (1) into second-quantized notation is given in the Supplemental Material (SM) [58]. Since this Hamiltonian is quadratic in creation and annihilation operators for magnons and phonons, it can be exactly diagonalized to obtain quasiparticle band structure in Figs. 2 for magnon-polaron quasiparticle. For easy comparison, Fig. 2(b) plots non-hybridized magnon (red curves) and phonon (blue curves) bands in the absence of magnetoelastic coupling [$H_m = 0$ in Eq. (4)] and for zero applied magnetic field [$B_z = 0$ in Eq. (2)].

B. Transverse thermal and spin transport in the linear response regime

Within the linear response theory, the equations describing transverse quasiparticle transport underlying

THE and SNE are given by [31, 47, 75–78]

$$j_y^Q = -\kappa_{xy}\partial_x T, \tag{7}$$
$$j_y^{S^z} = -\eta_{xy}^{S^z}\partial_x T, \tag{8}$$

where j_y^Q and $j_y^{S^z}$ are thermal and spin current, respectively, flowing along the y-axis in response to the temperature gradient $\partial_x T$ applied along the x-axis [Fig. 1]. The coefficients of proportionality in Eqs. (7) and (8) are the thermal Hall conductivity

$$\kappa_{xy} = -\frac{k_B^2 T}{\hbar}\sum_{n=1}^{N}\int F_2(\rho_n)\,\Omega_n^z d\boldsymbol{k}, \tag{9}$$

and the spin Nernst conductivity

$$\eta_{xy}^{S^z} = \frac{k_B}{\hbar}\sum_{n=1}^{N}\int F_1(\rho_n)\,\Omega_{S^z,n}^z d\boldsymbol{k}. \tag{10}$$

Here $\rho_n = [e^{E_n/k_B T} - 1]^{-1}$ is the Bose-Einstein distribution function, with E_n being the eigenenergy of the nth band, which enters into the conductivity expressions through functions

$$F_1(\rho_n) = (1+\rho_n)\,ln\,(1+\rho_n) - \rho_n ln\,(\rho_n)\,, \tag{11}$$

or

$$F_2(\rho_n) = (1+\rho_n)\ln^2\left(1+\frac{1}{\rho_n}\right) - \ln^2(\rho_n) - 2\mathrm{Li}_2(-\rho_n)\,, \tag{12}$$

where Li_2 is the polylogarithm function. Finally, the Berry $\boldsymbol{\Omega}_n(\boldsymbol{k})$ and spin (generalized) spin Berry $\boldsymbol{\Omega}_{S^\alpha,n}(\boldsymbol{k})$ curvature of the nth band are given by [31, 47]

$$\boldsymbol{\Omega}_n(\boldsymbol{k}) = \sum_{m\neq n}\frac{i\hbar^2\langle n(\boldsymbol{k})|\boldsymbol{v}|m(\boldsymbol{k})\rangle\langle m(\boldsymbol{k})|\boldsymbol{\sigma}_3|m(\boldsymbol{k})\rangle \times \langle m(\boldsymbol{k})|\boldsymbol{v}|n(\boldsymbol{k})\rangle\langle n(\boldsymbol{k})|\boldsymbol{\sigma}_3|n(\boldsymbol{k})\rangle}{\left[\sigma_3^{nn}E_n(\boldsymbol{k}) - \sigma_3^{mm}E_m(\boldsymbol{k})\right]^2}, \tag{13}$$

and

$$\boldsymbol{\Omega}_{S^\alpha,n}(\boldsymbol{k}) = \sum_{m\neq n}\frac{i\hbar^2\langle n(\boldsymbol{k})|\boldsymbol{j}^{S^\alpha}|m(\boldsymbol{k})\rangle\langle m(\boldsymbol{k})|\boldsymbol{\sigma}_3|m(\boldsymbol{k})\rangle \times \langle m(\boldsymbol{k})|\boldsymbol{v}|n(\boldsymbol{k})\rangle\langle n(\boldsymbol{k})|\boldsymbol{\sigma}_3|n(\boldsymbol{k})\rangle}{\left[\sigma_3^{nn}E_n(\boldsymbol{k}) - \sigma_3^{mm}E_m(\boldsymbol{k})\right]^2}, \tag{14}$$

where we use $E_n(\boldsymbol{k})$ and $|n(\boldsymbol{k})\rangle$ to denote the eigenvectors and eigenvalues, respectively, obtained from Colpa's diagonalization algorithm [79–82] (see the SM [58] for details); $\boldsymbol{v} = (v_x, v_y, v_z)$ denotes the velocity vector operator; $\boldsymbol{j}^{S^\alpha}$ denotes the spin current tensor operator

$$\boldsymbol{j}^{S^\alpha} = S^\alpha\boldsymbol{\sigma}_3\boldsymbol{v} + \boldsymbol{v}\boldsymbol{\sigma}_3 S^\alpha; \tag{15}$$

and $\boldsymbol{\sigma}_3$ matrix is given by

$$\boldsymbol{\sigma}_3 = \begin{pmatrix}\mathbf{1}_{N\times N} & 0\\ 0 & -\mathbf{1}_{N\times N}\end{pmatrix}, \tag{16}$$

where $\mathbf{1}_{N\times N}$ is $N\times N$ identity matrix and $\sigma_3^{nn} = \langle n(\boldsymbol{k})|\boldsymbol{\sigma}_3|n(\boldsymbol{k})\rangle$ is the nth diagonal element of $\boldsymbol{\sigma}_3$. Thus, evaluating Berry [Eqs. (13)] and spin Berry [Eq. (14)] curvatures directly yields the thermal and spin Nernst conductivities, respectively.

III. RESULTS AND DISCUSSION

A. Topological transport of magnon-polarons: Thermal Hall and spin Nernst effects

We first assume that $FePS_3$ is exposed to an applied magnetic field of 30 T. Figure 3(a) show a zoom onto magnon-phonon hybridized bands from Fig. 2 focused on 4th (predominantly magnon, as it is mostly red) and 5th (predominantly phonon, as it is mostly blue) band in the energy window between 10 and 20 meV along the X-Γ-M path. These two bands are strongly coupled, which results in two anticrossings [Fig. 3(a)]. In the vicinity of these anticrossings, the eigenstates are hybridized, $\psi_{\mathrm{hybrid}} = \psi_{\mathrm{magnon}} \pm \psi_{\mathrm{phonon}}$, with both magnon and phonon character. The presence of such superpositions are denoted by the bright green-yellow color of the bands in the anticrossing region [Fig. 3(a)]. We note that *both* an applied magnetic field and magnetoelastic coupling between magnons and phonons are required for such hybridization and anticrossing to emerge—the magnetoelastic coupling provides the necessary interaction, while the magnetic field tunes the magnon and phonon bands toward energy degeneracy.

The hybridization of two distinct excitations leads to a finite Berry curvature. Let us recall that, e.g., hybridization of s- and p-states in HgTe/CdTe semiconductor quantum wells causes nontrivial topological properties for electrons at the Fermi level [83]. The physics here is analogous—in the region of the BZ where the magnon band (4th band) and phonon band (5th band) anticross we expect nonzero Berry curvature. In contrast, we expect that away from the anticrossing regions,

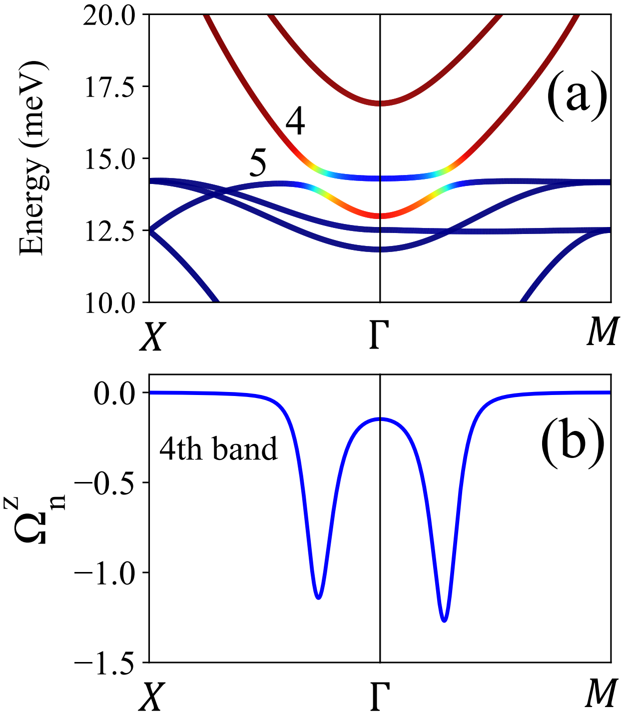

FIG. 3. (a) The hybridized magnon-phonon band structure of 2D $FePS_3$, along X-Γ-M high symmetry path, calculated for an applied magnetic field of $B_z = 30$ T. (b) The corresponding Berry curvature Ω^z_n along the X-Γ-M path calculated for the 4th band in panel (a).

the Berry curvature should vanish because either band is dominated solely by magnon or phonon character. Figure 3(b), showing the Berry curvature [Eq. 13] for the 4th band along the same X-Γ-M path, confirms this expectation as $\Omega^z_n(\boldsymbol{k}) \neq 0$ in Fig. 3(b) only around the anticrossing regions identified in Fig. 3(a). Thus, the nontrivial topology of magnon and phonon bands in $FePS_3$ emerges due to their hybridization via magnetoelastic coupling [Eq. (4)], while these bands individually [Fig. 2] exhibit trivial topology [Fig. 3(b)].

Figure 4 shows the Berry curvature for the eight bands 1–8 in Fig. 2 as a function of the in-plane wave vector $\boldsymbol{k} = (k_x, k_y)$. In each panel, we also report the Chern number calculated as

$$C_n = \frac{1}{2\pi} \int_{BZ} \Omega^z_n(\boldsymbol{k}) dk_x dk_y. \tag{17}$$

These calculations were performed for an applied magnetic field $B_z = 30\,T$ that causes the lowest magnon band to overlap with the out-of-plane optical phonon bands, as shown in Fig. 3(a). Non-zero Berry curvature is observed in the vicinity of anticrossing regions in the 4th, 5th, and 6th bands in the color plot. The 1st band [Fig. 4(a)] has zero Berry curvature everywhere, which obviously leads to zero Chern number. The 4th and 6th bands [Figs. 4(d) and 4(f)] have non-zero Berry curvature, but the integral of the Berry curvature over the entire BZ of these bands vanishes. As a result, the Chern number is zero and these are topologically trivial bands. The other bands all have nonzero Chern number, with the sum of their Chern numbers obeying the sum rule, $\sum_{i=1}^{N} C_i = 0$, as expected for a Bogoliubov-de Gennes (BdG) Hamiltonian [28] (see the SM [58] for more details on the BdG Hamiltonian construction). The bands with nonzero Chern number will contribute to THE via Eq. (9).

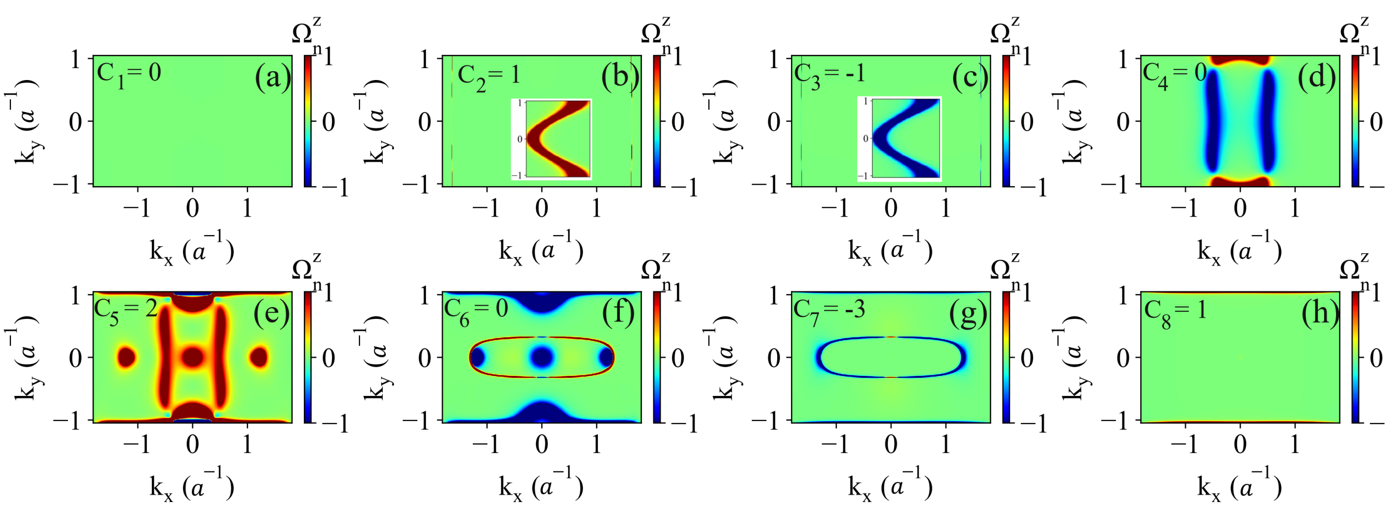

FIG. 4. The Berry curvature Ω^z_n [Eq. (13)] computed for magnon-phonon bands [Fig. 2] of $FePS_3$ as a function of the in-plane wavevector (k_x, k_y) within the first BZ and using applied magnetic field $B_z = 30$ T. Panels (a)–(h) correspond to bands 1–8 denoted in Fig. 2. Their corresponding Chern number C_n $(n = 1, 2, ..., 8)$ in Eq. (17) is provided in the upper left corner of each panel. The insets in panels (b) and (c) show a zoom in around $k_x = -1.64\ a^{-1}$ where the Berry curvature of the corresponding bands is nonzero.

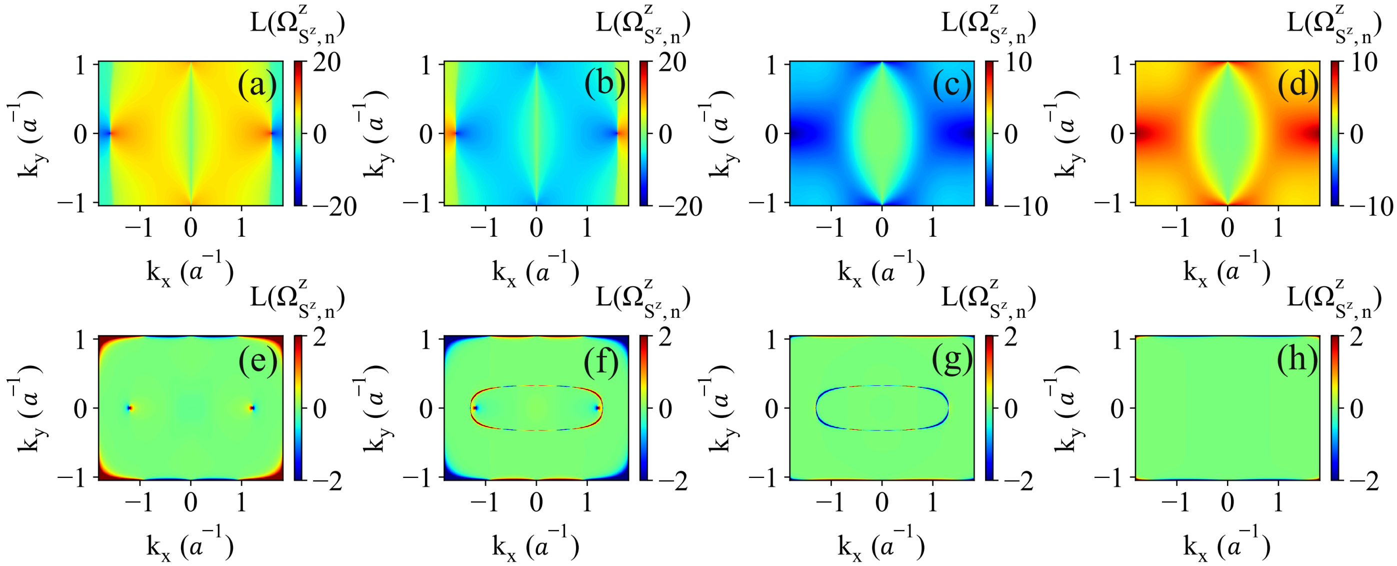

FIG. 5. The *spin* Berry curvature $\Omega^z_{S_z,n}$ [Eq. (14)] computed for magnon-phonon bands [Fig. 2] of $FePS_3$ as a function of the in-plane wavevector (k_x, k_y) within the first BZ and using in the absence of applied magnetic field $B_z = 0$. Panels (a)–(h) correspond to bands 1–8 denoted in Fig. 2. The color bar encodes the magnitude of the function $L = \mathrm{sgn}(\Omega^z_{S^z,n}) \log(1+|\Omega^z_{S^z,n}|)$.

However, it is surprising and quite different from standard lore [27–30] that non-zero Berry curvature can be found for the 2nd [Fig. 4(b)], 3rd [Fig. 4(c)] and 8th [Fig. 4(h)] band because these bands are well above or well below the energy window in which magnon and phonon bands become degenerate in energy and anticross [Fig. 2]. These bands all have non-trivial topology with a Chern number equal to ±1. The finite Berry curvature and nontrivial topological properties of these bands can be understood as follows. Magnetoelastic interaction facilitates coupling between magnon and phonon bands even when they are *not* energetically close together, so that magnon bands have small phononic character and vice versa [31]. This effect can open a gap between two magnon-like bands [such as 2nd and 3rd in Figs. 4(b) and 4(c)] at $k_x = \pm 1.64$ (a^{-1}), thereby making possible interband transitions between these two [see the inset of Fig. S2(b) in the SM [58] for details]. Without magnetoelastic coupling, these magnon bands are degenerate, i.e., they cross each other at $k_x = \pm 1.64$ (a^{-1}) [Fig. S2(a) in the SM [58]]. Precise quantum-mechanical interpretation of this picture can be obtained from the perturbation theory—the gap opening between the two magnon-like bands is due to perturbations from phonons, which appears as a second order correction term

$$\delta E^m_{ij} \propto \sum_p \left[\bar{H}\right]_{mi,p} \left[\bar{H}\right]_{p,mj} \left[\frac{1}{\bar{E}_{mi} - \bar{E}_p} + \frac{1}{\bar{E}_{mj} - \bar{E}_p}\right] \tag{18}$$

to the magnon band levels [for derivation of Eq. (18) see the SM [58]]. Here the indices p, mi, mj indicate the phonon states which mediate interband transitions between magnon states i and j; $\left[\bar{H}\right]_{mi,p}$ ($\left[\bar{H}\right]_{p,mj}$) describes the coupling between i magnon (phonon) band and phonon (j magnon) states; $\bar{E}_{mi}$, $\bar{E}_{mj}$ and $\bar{E}_p$ are eigenenergies of i magnon, j magnon, and phonon states, respectively, as obtained from exact diagonalization of the bosonic magnon-phonon Hamiltonian (see the SM [58] for details). As the result, the Berry curvature of the 2nd and 3rd band at around $k_x = \pm 1.64$ (a^{-1}), which is associated with the tiny avoided crossing points between the 2nd and 3rd magnon-like bands, *becomes finite*. An analogous effect occurs for the phonon bands. For instance, a magnon-mediated phonon-phonon interband transition between 7th and 8th bands in Fig. 2(a) generates a finite Berry curvature at $k_y \approx \pm 1$ (a^{-1}) for the 8th (phonon-like) band, as confirmed by Fig. 4(h).

Another consequence of these phonon-mediated magnon-magnon and magnon-mediated phonon-phonon interband transitions is that they induce the topological transverse transport of spin angular momentum carried by magnons even at *zero* applied magnetic field. Figure 5 shows the computed spin (generalized) Berry curvature [Eq. (5)] for bands 1–8 [Fig. 2] calculated for $B_z = 0$. We note that in the absence of both applied magnetic field and magnon-phonon coupling, the magnon bands exhibit a double degeneracy, with one set of bands carrying spin up [such as the 1st band in Fig. 2(a)] and another set carrying spin down [such as the 2nd band in Fig. 2(a)]. Consequently, the band structures of the magnon-phonon system in $FePS_3$ also exhibit a double degeneracy, as illustrated in Fig. 2(b). However, the magnetoelastic coupling between the magnetic and elastic degrees of freedom in $FePS_3$ lifts the degeneracy of these two magnon bands with opposite spin, therefore mak-

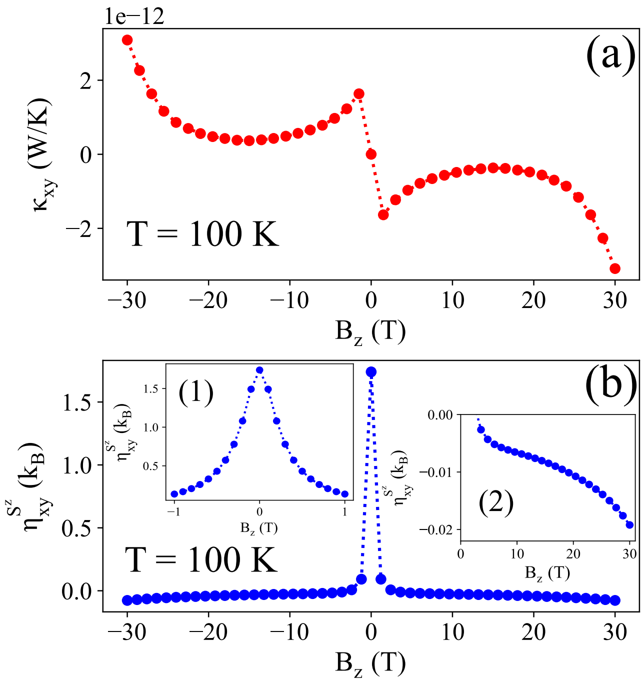

FIG. 6. (a) Thermal Hall and (b) spin Nernst conductivities as a function of an applied magnetic field B_z. These conductivities are calculated at $T = 100$ K using $FePS_3$ magnon-phonon band structure [Fig. 2] and its Berry [Fig. 4] and spin Berry [Fig. 5] curvatures. Two insets in panel (b) show a zoom in for: (1) $B_z \in [-1\ \text{T}, 1\ \text{T}]$; and (2) $B_z \in [2\ \text{T}, 30\ \text{T}]$.

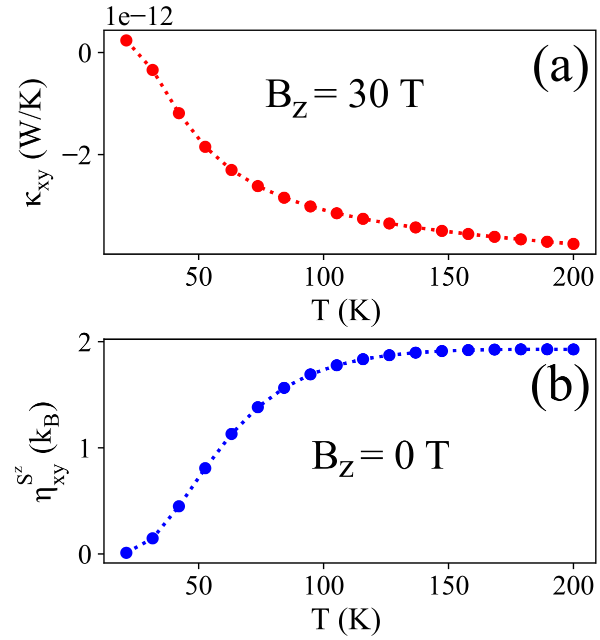

FIG. 7. (a) Thermal Hall and (b) spin Nernst conductivities of $FePS_3$ as a function of temperature T calculated for applied magnetic field $B_z = 30$ T in (a) or $B_z = 0$ T in (b).

ing possible for interband transition between those two magnon-like bands of opposite spin, even in the absence an applied magnetic field (see the SM [58] for Fig. S3 and details of calculations). Such phonon-mediated interband transitions between magnon-like bands, which are energetically distant from usually considered [27–30] anticrossing regions [Fig. 3(a)] of hybridized magnon-phonon bands, can result in a very large spin Berry curvature found in Fig. 5(a)–(d) because of the smallness [31] [with respect to the gap in anticrossing regions in Fig. 3(a)] of energy gap between the two magnon-like bands with opposite spin polarization [Fig. S3(b) in SM [58]]. The same effect can operate between phonon-like bands. For example, the 7th and 8th (phonon-like) bands in Fig. 2(a) will exhibit magnon-mediated interband transitions, thereby developing finite spin Berry curvature [Figs. 5(g) and 5(h)].

B. Magnetic field dependence of the thermal Hall and spin Nernst effects on applied magnetic field

Using computed Berry [Fig. 4] and spin Berry [Fig. 5] curvatures, we can obtain directly thermal Hall [via Eq. (9)] and spin Hall [via Eq. (10)] conductivities shown in Figs. 6(a) and 6(b), respectively as a function of applied magnetic field at fixed temperature $T = 100$ K that is below the Néel temperature of $FePS_3$. As expected, the thermal Hall conductivity changes sign when we reverse the applied magnetic field, i.e., $\kappa_{xy}(B_z) = -\kappa_{xy}(-B_z)$. In the absence of applied magnetic field [$B_z = 0$ point in Fig. 6(a)], the thermal Hall conductivity vanishes. We can understand this feature by recognizing that when the applied magnetic field is absent, the system will be invariant under the time-reversal symmetry operation $\mathcal{T}$ combined with the spin rotation symmetry operation $\mathcal{C}$ that flips all spins in the system. The combination of these operations leads to an effective time reversal symmetry (TRS) operation $\mathcal{T}' = \mathcal{T}\mathcal{C}$ under which $\partial_x T$ is preserved while the thermal Hall current is transformed as $j_y^Q \to -j_y^Q$. Because this system preserves $\mathcal{T}' = \mathcal{T}\mathcal{C}$ symmetry, $j_y^Q = -j_y^Q = 0$ and the thermal Hall conductivity κ_{xy} must be zero. We note that even though the thermal Hall conductivity κ_{xy} of the magnon-phonon hybridized system is zero in zero magnetic field, the Berry curvature $\Omega_n^z(\boldsymbol{k})$ of individual bands may be finite at specific k-points within the BZ, as long as the integral of the Berry curvature over the entire BZ vanishes (see the SM [58] for a detailed argument). This ensures that THE induced by the magnon-phonon hybridization does not occur without breaking the effective TRS [29].

In contrast to the thermal Hall conductivity, the spin Nernst conductivity shown in Fig. 6(b) is an even function of B_z, i.e., $\eta_{xy}^{S^z}(B_z) = \eta_{xy}^{S^z}(-B_z)$. Moreover, spin Nernst conductivity be finite even in the absence of an applied magnetic field [31], i.e., under the effective time reversal symmetry $\mathcal{T}'$. Indeed, if we rewrite the thermal spin current [Eq. (8)] as $j_y^{S^z} = j_y^{S^{z\uparrow}} - j_y^{S^{z\downarrow}}$, then under $\mathcal{T}'$ operation the spin-polarized currents on the right side change the sign and flip the spin, i.e., $\mathcal{T}' j_y^{S^{z\uparrow}} = -j_y^{S^{z\downarrow}}$ and $\mathcal{T}' j_y^{S^{z\downarrow}} = -j_y^{S^{z\uparrow}}$. This leads to $\mathcal{T}' j_y^{S^z} = -j_y^{S^{z\downarrow}} + j_y^{S^{z\uparrow}} = j_y^{S_z}$, which is always true because our system preserves the effective time reversal symmetry in the absence of an applied magnetic field. It is therefore possible for the spin Nernst conductivity to be nonzero at zero applied magnetic field, as confirmed in Fig. 6(b). At zero or small applied magnetic field, the *giant* spin Nernst conductivity is mainly governed by phonon-mediated interband transitions between magnon-like bands. It then decays rapidly [inset (1) in Fig. 6] when the applied magnetic field is $B_z \gtrsim 2$ T, dropping eventually by two orders of magnitude, because the energy spacing between the two magnon-like bands increases and thus interband transitions between the two are suppressed.

As the applied magnetic field magnitude increases from ≈ 2 to 30 T the spin Nernst conductivity slightly changes while becoming negative, $\eta_{xy}^{S^z} < 0$ [inset (2) in Fig. 6]. We find that from ≈ 2 to ≈ 5 T, the spin Nernst conductivity originates primarily from magnon-mediated interband transitions between phonon-like bands. Once the phonon bands start hybridizing with magnon bands at $B_z \approx 5$ T, spin Berry curvature [Fig. 3] at anticrossing regions of magnon-phonon bands also contribute, as amply explored in prior literature [27–30]. To understand why the spin Nernst conductivity becomes more negative with increasing applied magnetic field, we consider that in the conserved spin approximation the spin Nernst conductivity derived from semi-classical theory is given by [28, 55, 75]:

$$\eta_{xy}^{S^z} = -\frac{k_B}{\hbar V} \sum_k \sum_{n=1}^{N} \langle S^z \rangle \Omega_n^z F_1(E_n/k_B T) \tag{19}$$

where $\langle S^z \rangle$ is the expectation value of S^z operator, Ω_n^z is the Berry curvature of the *nth* band and the F_1 function was defined in Eq. 11. From Eq. (19), we see that increasing applied magnetic field leads to both larger spin polarization and stronger hybridizations between magnon and phonon states due to the shift toward energy degeneracy of the magnon and phonon states. Consequently, the amplitude of the spin Nernst conductivity $\eta_{xy}^{S^z}$ is augmented within this regime.

Since the computed spin Nernst conductivity of $FePS_3$ around zero applied magnetic field is two orders of magnitude [Fig. 6] larger than at $B_z \approx 10$ T, it should be possible to experimentally probe this effect by sweeping magnetic field. Furthermore, we note that spin Nernst conductivity of $FePS_3$ is much larger than that of other recently investigated 2D transition phosphorus trichalcogenides materials, such as $MnPS_3$, $NiPS_3$, $NiPSe_3$. Specifically, for $FePS_3$ in the zigzag phase studied here, the computed spin Nernst conductivity is about four orders of magnitude larger than that of $MnPS_3$ in the Néel phase [30].

We also emphasize that in the absence of magnetoelastic coupling, both the thermal Hall and spin Nernst conductivities vanish, irrespective of the applied magnetic field. This is because the system without magnetoelastic coupling preserves $\mathcal{T}_a\mathcal{M}_y$ symmetry, where $\mathcal{M}_y$ is the mirror symmetry about the plane normal to the y-axis and $\mathcal{T}_a$ is a translation operator that moves the system by the vector $\boldsymbol{\beta}_2$ [Fig. 1]. Unlike the effective time reversal symmetry $\mathcal{T}'$, $\mathcal{T}_a\mathcal{M}_y$ does not change the spin direction but does change the sign of both the thermal Hall and thermal spin Nernst current. In other words, one must have $j_y^Q = -j_y^Q = 0$ and $j_y^{S^z} = -j_y^{S^z} = 0$, therefore both the thermal Hall and spin Nernst conductivity must be zero. It is only when the magnetoelastic interaction breaks $\mathcal{T}_a\mathcal{M}_y$ symmetry that one obtains finite topological transverse transport of quasiparticles and their spin in a 2D AFM material.

Finally, Fig. 7 shows the thermal Hall and spin Nernst conductivities as a function of temperature using $B_z = 30$ T or $B_z = 0$ applied magnetic field, respectively. Both conductivities increase in magnitude with increasing temperature because there are increasing contributions to Berry and spin Berry curvature from phonon and magnon bands at higher energy. They start to saturate at $T \simeq 100$ K when all magnon bands at higher energy have already been included. We note that when $T \simeq 0$ K, the spin Nernst conductivity is almost zero, while the thermal Hall conductivity changes from positive to negative. This is because at very low temperature the main contributions to the THE come from the acoustic phonon band [8th band in Fig. 2(a)] with positive Chern number $C_8 = 1$ [Fig. 4(h)]. As the temperature increases even slightly, the other bands with negative Chern number begin to contribute to topological transverse transport of quasiparticle and, thus, the thermal Hall conductivity becomes negative. In contrast, even though the spin Berry curvature of the lowest phonon-like band [8th band in Fig. 2(a)] is finite, the sum of the spin Berry curvature of the 8th band over the entire BZ vanishes to yield $\eta_{xy}^{S^z} \to 0$ at zero temperature.

IV. CONCLUSIONS

In conclusion, we have investigated the transverse topological transport of magnon-polaron quasiparticles in the zigzag phase of $FePS_3$ 2D AFM. While we reproduce previous findings [27–30], obtained for different realizations of 2D AFMs, on magnetoelastic coupling mechanism where anticrossing regions of hybridized magnons-phonon bands provide key contribution [28] to THE and SNE, we also predict giant spin Nernst current carried by magnons even in zero applied magnetic field. This surprising finding was noticed before [31], but here we explain it thoroughly by using perturbative Eq. (18) which reveals principal contribution to the spin Berry curvature behind SNE coming from interband transition between slightly gapped magnon-like bands that are far away in energy from usually considered anticrossing regions [27–30]. Of relevance to experimental probing of THE and

SNE, which are currently lacking [27], our analysis indicates that $FePS_3$ will exhibit sizable thermal Hall conductivity and giant spin Nernst conductivities at temperatures of $T \simeq 100$ K, which is still below its Néel temperature $T_N \approx 118$ K [49, 84].

ACKNOWLEDGMENTS

This research was primarily supported by NSF through the University of Delaware Materials Research Science and Engineering Center, DMR-2011824.

[1] M. Gibertini, M. Koperski, A. F. Morpurgo, and K. S. Novoselov, Magnetic 2D materials and heterostructures, Nat. Nanotech. **14**, 408 (2019).

[2] M. B. Jungfleisch, W. Zhang, and A. Hoffmann, Perspectives of antiferromagnetic spintronics, Phys. Lett. A **382**, 865 (2018).

[3] L. Hao, D. Meyers, H. Suwa, J. Yang, C. Frederick, T. R. Dasa, G. Fabbris, L. Horak, D. Kriegner, Y. Choi, *et al.*, Giant magnetic response of a two-dimensional antiferromagnet, Nat. Phys. **14**, 806 (2018).

[4] B. Huang, M. A. McGuire, A. F. May, D. Xiao, P. Jarillo-Herrero, and X. Xu, Emergent phenomena and proximity effects in two-dimensional magnets and heterostructures, Nat. Mater. **19**, 1276 (2020).

[5] K. Dolui, M. D. Petrovic, K. Zollner, P. Plechac, J. Fabian, and B. K. Nikolić, Proximity spin–orbit torque on a two-dimensional magnet within van der Waals heterostructure: Current-driven antiferromagnet-to-ferromagnet reversible nonequilibrium phase transition in bilayer CrI_3, Nano Lett. **20**, 2288 (2020).

[6] S. Yang, T. Zhang, and C. Jiang, van der Waals magnets: Material family, detection and modulation of magnetism, and perspective in spintronics, Adv. Sci. **8**, 2002488 (2021).

[7] X. Jiang, Q. Liu, J. Xing, N. Liu, Y. Guo, Z. Liu, and J. Zhao, Recent progress on 2D magnets: Fundamental mechanism, structural design and modification, Appl. Phys. Rev. **8**, 031305 (2021).

[8] X. Tan, L. Ding, G.-F. Du, and H.-H. Fu, Spin caloritronics in two-dimensional $CrI_3/NiCl_2$ van der Waals heterostructures, Phys. Rev. B **103**, 115415 (2021).

[9] M.-H. Phan, M. T. Trinh, T. Eggers, V. Kalappattil, K.-i. Uchida, L. M. Woods, and M. Terrones, A perspective on two-dimensional van der Waals opto-spin-caloritronics, Appl. Phys. Lett. **119**, 250501 (2021).

[10] D. Xiong, Y. Jiang, K. Shi, A. Du, Y. Yao, Z. Guo, D. Zhu, K. Cao, S. Peng, W. Cai, *et al.*, Antiferromagnetic spintronics: An overview and outlook, Fundam. Res. **2**, 522 (2022).

[11] A. Suresh, U. Bajpai, and B. K. Nikolić, Magnon-driven chiral charge and spin pumping and electron-magnon scattering from time-dependent quantum transport combined with classical atomistic spin dynamics, Phys. Rev. B **101**, 214412 (2020).

[12] X.-X. Zhang, L. Li, D. Weber, J. Goldberger, K. F. Mak, and J. Shan, Gate-tunable spin waves in antiferromagnetic atomic bilayers, Nat. Mater. **19**, 838 (2020).

[13] A. Suresh, U. Bajpai, M. D. Petrović, H. Yang, and B. K. Nikolić, Magnon- versus electron-mediated spin-transfer torque exerted by spin current across an antiferromagnetic insulator to switch the magnetization of an adjacent ferromagnetic metal, Phys. Rev. Appl. **15**, 034089 (2021).

[14] U. Bajpai, A. Suresh, and B. K. Nikolić, Quantum many-body states and Green's functions of nonequilibrium electron-magnon systems: Localized spin operators versus their mapping to Holstein-Primakoff bosons, Phys. Rev. B **104**, 184425 (2021).

[15] C. A. Belvin, E. Baldini, I. O. Ozel, D. Mao, H. C. Po, C. J. Allington, S. Son, B. H. Kim, J. Kim, I. Hwang, *et al.*, Exciton-driven antiferromagnetic metal in a correlated van der Waals insulator, Nat. Commun. **12**, 4837 (2021).

[16] A. V. Chumak, P. Kabos, M. Wu, C. Abert, C. Adelmann, A. Adeyeye, J. Åkerman, F. G. Aliev, A. Anane, A. Awad, *et al.*, Advances in magnetics roadmap on spin-wave computing, IEEE Trans. Magn. **58**, 1 (2022).

[17] J. Li, H. T. Simensen, D. Reitz, Q. Sun, W. Yuan, C. Li, Y. Tserkovnyak, A. Brataas, and J. Shi, Observation of magnon polarons in a uniaxial antiferromagnetic insulator, Phys. Rev. Lett. **125**, 217201 (2020).

[18] R. Yahiro, T. Kikkawa, R. Ramos, K. Oyanagi, T. Hioki, S. Daimon, and E. Saitoh, Magnon polarons in the spin peltier effect, Phys. Rev. B **101**, 024407 (2020).

[19] N. Vidal-Silva, E. Aguilera, A. Roldán-Molina, R. A. Duine, and A. S. Nunez, Magnon polarons induced by a magnetic field gradient, Phys. Rev. B **102**, 104411 (2020).

[20] S. M. Tabatabaei, R. A. Duine, and B. Zare Rameshti, Magnon-polaron anomaly in nonlocal spin transport through antiferromagnetic insulators, Phys. Rev. B **104**, 014432 (2021).

[21] T. Kikkawa, K. Oyanagi, T. Hioki, M. Ishida, Z. Qiu, R. Ramos, Y. Hashimoto, and E. Saitoh, Composition-tunable magnon-polaron anomalies in spin Seebeck effects in epitaxial $Bi_xY_{3-x}Fe_5O_{12}$ films, Phys. Rev. Mater. **6**, 104402 (2022).

[22] W. Chen and M. Sigrist, Dissipationless multiferroic magnonics, Phys. Rev. Lett. **114**, 157203 (2015).

[23] T. Nomura, X.-X. Zhang, S. Zherlitsyn, J. Wosnitza, Y. Tokura, N. Nagaosa, and S. Seki, Phonon magnetochiral effect, Phys. Rev. Lett. **122**, 145901 (2019).

[24] C. Zhao, Y. Li, Z. Zhang, M. Vogel, J. E. Pearson, J. Wang, W. Zhang, V. Novosad, Q. Liu, and A. Hoffmann, Phonon transport controlled by ferromagnetic resonance, Phys. Rev. Appl. **13**, 054032 (2020).

[25] J. Holanda, D. S. Maior, O. A. Santos, A. Azevedo, and S. M. Rezende, Evidence of phonon pumping by magnonic spin currents, Appl. Phys. Lett. **118**, 022409 (2021).

[26] S. M. Rezende, D. S. Maior, O. Alves Santos, and J. Holanda, Theory for phonon pumping by magnonic spin currents, Phys. Rev. B **103**, 144430 (2021).

[27] H. Zhang and R. Cheng, A perspective on magnon spin Nernst effect in antiferromagnets, Appl. Phys. Lett. **120**, 090502 (2022).

[28] S. Park, N. Nagaosa, and B.-J. Yang, Thermal Hall effect, spin Nernst effect, and spin density induced by a thermal

gradient in collinear ferrimagnets from magnon-phonon interaction, Nano Lett. **20**, 2741 (2020).
[29] S. Zhang, G. Go, K.-J. Lee, and S. K. Kim, SU(3) topology of magnon-phonon hybridization in 2D antiferromagnets, Phys. Rev. Lett. **124**, 147204 (2020).
[30] N. Bazazzadeh, M. Hamdi, S. Park, A. Khavasi, S. M. Mohseni, and A. Sadeghi, Magnetoelastic coupling enabled tunability of magnon spin current generation in two-dimensional antiferromagnets, Phys. Rev. B **104**, L180402 (2021).
[31] G. Go and S. K. Kim, Tunable large spin Nernst effect in a two-dimensional magnetic bilayer, Phys. Rev. B **106**, 125103 (2022).
[32] Q. Zhang, M. Ozerov, E. V. Boström, J. Cui, N. Suri, Q. Jiang, C. Wang, F. Wu, K. Hwangbo, J.-H. Chu, *et al.*, Coherent strong-coupling of terahertz magnons and phonons in a van der Waals antiferromagnetic insulator, arXiv preprint 10.48550/arXiv.2108.11619 (2021).
[33] J. Luo, S. Li, Z. Ye, R. Xu, H. Yan, J. Zhang, G. Ye, L. Chen, D. Hu, X. Teng, W. A. Smith, B. I. Yakobson, P. Dai, A. H. Nevidomskyy, R. He, and H. Zhu, Evidence for topological magnon–phonon hybridization in a 2D antiferromagnet down to the monolayer limit, Nano Lett. **23**, 2023 (2023).
[34] M. Xu, J. Puebla, F. Auvray, B. Rana, K. Kondou, and Y. Otani, Inverse edelstein effect induced by magnon-phonon coupling, Phys. Rev. B **97**, 180301 (2018).
[35] F. Godejohann, A. V. Scherbakov, S. M. Kukhtaruk, A. N. Poddubny, D. D. Yaremkevich, M. Wang, A. Nadzeyka, D. R. Yakovlev, A. W. Rushforth, A. V. Akimov, and M. Bayer, Magnon polaron formed by selectively coupled coherent magnon and phonon modes of a surface patterned ferromagnet, Phys. Rev. B **102**, 144438 (2020).
[36] C. R. Berk and H. Schmidt, A quantum tango between magnons and phonons, Physics **13**, 167 (2020).
[37] D. Bozhko, V. Vasyuchka, A. Chumak, and A. Serga, Magnon-phonon interactions in magnon spintronics, Low Temp. Phys. **46**, 383 (2020).
[38] D. D. Awschalom, C. R. Du, R. He, F. J. Heremans, A. Hoffmann, J. Hou, H. Kurebayashi, Y. Li, L. Liu, V. Novosad, *et al.*, Quantum engineering with hybrid magnonic systems and materials, IEEE Transactions on Quantum Engineering **2**, 1 (2021).
[39] Y. Li, C. Zhao, W. Zhang, A. Hoffmann, and V. Novosad, Advances in coherent coupling between magnons and acoustic phonons, APL Mater. **9**, 060902 (2021).
[40] F. Mertens, D. Mönkebüscher, U. Parlak, C. Boix-Constant, S. Mañas-Valero, M. Matzer, R. Adhikari, A. Bonanni, E. Coronado, A. M. Kalashnikova, *et al.*, Ultrafast coherent thz lattice dynamics coupled to spins in the van der Waals antiferromagnet $FePS_3$, Adv. Mater. **35**, 2208355 (2023).
[41] V. A. Zyuzin and A. A. Kovalev, Magnon spin Nernst effect in antiferromagnets, Phys. Rev. Lett. **117**, 217203 (2016).
[42] R. Takahashi and N. Nagaosa, Berry curvature in magnon-phonon hybrid systems, Phys. Rev. Lett. **117**, 217205 (2016).
[43] S. Murakami and A. Okamoto, Thermal Hall effect of magnons, J. Phys. Soc. Jpn **86**, 011010 (2017).
[44] G. Go, S. K. Kim, and K.-J. Lee, Topological magnon-phonon hybrid excitations in two-dimensional ferromagnets with tunable Chern numbers, Phys. Rev. Lett. **123**, 237207 (2019).
[45] X. Zhang, Y. Zhang, S. Okamoto, and D. Xiao, Thermal Hall effect induced by magnon-phonon interactions, Phys. Rev. Lett. **123**, 167202 (2019).
[46] A. Okamoto, S. Murakami, and K. Everschor-Sitte, Berry curvature for magnetoelastic waves, Phys. Rev. B **101**, 064424 (2020).
[47] B. Li, S. Sandhoefner, and A. A. Kovalev, Intrinsic spin Nernst effect of magnons in a noncollinear antiferromagnet, Phys. Rev. Res. **2**, 013079 (2020).
[48] B. Ma and G. A. Fiete, Antiferromagnetic insulators with tunable magnon-polaron Chern numbers induced by in-plane optical phonons, Phys. Rev. B **105**, L100402 (2022).
[49] S. Liu, A. Granados del Águila, D. Bhowmick, C. K. Gan, T. Thu Ha Do, M. A. Prosnikov, D. Sedmidubský, Z. Sofer, P. C. M. Christianen, P. Sengupta, and Q. Xiong, Direct observation of magnon-phonon strong coupling in two-dimensional antiferromagnet at high magnetic fields, Phys. Rev. Lett. **127**, 097401 (2021).
[50] D. Vaclavkova, M. Palit, J. Wyzula, S. Ghosh, A. Delhomme, S. Maity, P. Kapuscinski, A. Ghosh, M. Veis, M. Grzeszczyk, C. Faugeras, M. Orlita, S. Datta, and M. Potemski, Magnon polarons in the van der Waals antiferromagnet $FePS_3$, Phys. Rev. B **104**, 134437 (2021).
[51] A. Pawbake, T. Pelini, A. Delhomme, D. Romanin, D. Vaclavkova, G. Martinez, M. Calandra, M.-A. Measson, M. Veis, M. Potemski, *et al.*, High-pressure tuning of magnon-polarons in the layered antiferromagnet $FePS_3$, ACS Nano **16**, 12656 (2022).
[52] Y.-J. Sun, J.-M. Lai, S.-M. Pang, X.-L. Liu, P.-H. Tan, and J. Zhang, Magneto-Raman study of magnon–phonon coupling in two-dimensional Ising antiferromagnetic $FePS_3$, J. Phys. Chem. Lett. **13**, 1533 (2022).
[53] J. Sinova, S. O. Valenzuela, J. Wunderlich, C. H. Back, and T. Jungwirth, Spin Hall effects, Rev. Mod. Phys. **87**, 1213 (2015).
[54] B. K. Nikolić, L. P. Zârbo, and S. Souma, Imaging mesoscopic spin Hall flow: Spatial distribution of local spin currents and spin densities in and out of multiterminal spin-orbit coupled semiconductor nanostructures, Phys. Rev. B **73**, 075303 (2006).
[55] R. Cheng, S. Okamoto, and D. Xiao, Spin Nernst effect of magnons in collinear antiferromagnets, Phys. Rev. Lett. **117**, 217202 (2016).
[56] S. E. Hog, H. T. Diep, and H. Puszkarski, Theory of magnons in spin systems with Dzyaloshinskii-Moriya interaction, J. Phys.: Condens. Matter **29**, 305001 (2017).
[57] A. Mook, R. R. Neumann, J. Henk, and I. Mertig, Spin Seebeck and spin Nernst effects of magnons in noncollinear antiferromagnetic insulators, Phys. Rev. B **100**, 100401 (2019).
[58] See Supplemental Material at `https://mrsec.udel.edu/publications/`, which includes Refs. [85–94], for: (*i*) magnon-phonon Hamiltonian in the second-quantization formalism and details of its exact diagonalization; (*ii*) physical interpretation of the gap opening [Eq. (18)] between two magnon-like bands energetically distant from anticrossing regions, as found in exact diagonalization, by using perturbation from phonons onto magnons examined via the Löwdin partitioning; and (*iii*) additional details of Berry and spin Berry curvature calculations and related symmetry arguments.

[59] T. Olsen, Theory and simulations of critical temperatures in CrI_3 and other 2D materials: easy-axis magnetic order and easy-plane Kosterlitz-Thouless transitions, MRS Commun. **9**, 1142 (2019).

[60] J. Vanherck, C. Bacaksiz, B. Sorée, M. V. Milošević, and W. Magnus, 2D ferromagnetism at finite temperatures under quantum scrutiny, Appl. Phys. Lett. **117**, 052401 (2020).

[61] T. Olsen, Magnetic anisotropy and exchange interactions of two-dimensional $FePS_3$, $NiPS_3$ and $MnPS_3$ from first principles calculations, J. Phys. D: Appl. Phys. **54**, 314001 (2021).

[62] K.-Z. Du, X.-Z. Wang, Y. Liu, P. Hu, M. I. B. Utama, C. K. Gan, Q. Xiong, and C. Kloc, Weak van der Waals stacking, wide-range band gap, and raman study on ultrathin layers of metal phosphorus trichalcogenides, ACS Nano **10**, 1738 (2016).

[63] J.-U. Lee, S. Lee, J. H. Ryoo, S. Kang, T. Y. Kim, P. Kim, C.-H. Park, J.-G. Park, and H. Cheong, Ising-type magnetic ordering in atomically thin $FePS_3$, Nano Lett. **16**, 7433 (2016).

[64] J. Cui, E. V. Bostroem, M. Ozerov, F. Wu, Q. Jiang, J.-H. Chu, C. Li, F. Liu, X. Xu, A. Rubio, *et al.*, Chirality selective magnon-phonon hybridization and magnon-induced chiral phonons in an atomically thin antiferromagnet, arXiv preprint 10.48550/arXiv.2302.10656 (2023).

[65] A. Wildes, K. C. Rule, R. Bewley, M. Enderle, and T. J. Hicks, The magnon dynamics and spin exchange parameters of $FePS_3$, J. Phys.: Condens. Matter **24**, 416004 (2012).

[66] D. Lançon, H. C. Walker, E. Ressouche, B. Ouladdiaf, K. C. Rule, G. J. McIntyre, T. J. Hicks, H. M. Rønnow, and A. R. Wildes, Magnetic structure and magnon dynamics of the quasi-two-dimensional antiferromagnet $FePS_3$, Phys. Rev. B **94**, 214407 (2016).

[67] D. Q. To, W. Wu, S. Bhatt, Y. Liu, A. Janotti, J. M. O. Zide, M. J. H. Ku, J. Q. Xiao, M. B. Jungfleisch, S. Law, and M. F. Doty, Phonon-mediated strong coupling between a three-dimensional topological insulator and a two-dimensional antiferromagnetic material, Phys. Rev. Mater. **7**, 045201 (2023).

[68] R. Basnet, K. M. Kotur, M. Rybak, C. Stephenson, S. Bishop, C. Autieri, M. Birowska, and J. Hu, Controlling magnetic exchange and anisotropy by nonmagnetic ligand substitution in layered MPX_3 (M=Ni, Mn; X=S, Se, Phys. Rev. Res. **4**, 023256 (2022).

[69] K. Zollner and J. Fabian, Proximity effects in graphene on monolayers of transition-metal phosphorus trichalcogenides MPX_3 (M=Mn, Fe, Ni, Co, and X=S, Se), Phys. Rev. B **106**, 035137 (2022).

[70] Y. Lee, S. Son, C. Kim, S. Kang, J. Shen, M. Kenzelmann, B. Delley, T. Savchenko, S. Parchenko, W. Na, *et al.*, Giant magnetic anisotropy in the atomically thin van der Waals antiferromagnet $FePS_3$, Adv. Electron. Mater. **9**, 2200650 (2022).

[71] P. Shen and S. K. Kim, Magnetic field control of topological magnon-polaron bands in two-dimensional ferromagnets, Phys. Rev. B **101**, 125111 (2020).

[72] C. Kittel, Interaction of spin waves and ultrasonic waves in ferromagnetic crystals, Phys. Rev. **110**, 836 (1958).

[73] H. T. Simensen, R. E. Troncoso, A. Kamra, and A. Brataas, Magnon-polarons in cubic collinear antiferromagnets, Phys. Rev. B **99**, 064421 (2019).

[74] T. Sato, W. Yu, S. Streib, and G. E. W. Bauer, Dynamic magnetoelastic boundary conditions and the pumping of phonons, Phys. Rev. B **104**, 014403 (2021).

[75] R. Matsumoto and S. Murakami, Theoretical prediction of a rotating magnon wave packet in ferromagnets, Phys. Rev. Lett. **106**, 197202 (2011).

[76] R. Shindou, J. Ohe, R. Matsumoto, S. Murakami, and E. Saitoh, Chiral spin-wave edge modes in dipolar magnetic thin films, Phys. Rev. B **87**, 174402 (2013).

[77] R. Shindou, R. Matsumoto, S. Murakami, and J. Ohe, Topological chiral magnonic edge mode in a magnonic crystal, Phys. Rev. B **87**, 174427 (2013).

[78] R. Matsumoto, R. Shindou, and S. Murakami, Thermal Hall effect of magnons in magnets with dipolar interaction, Phys. Rev. B **89**, 054420 (2014).

[79] J. H. P. Colpa, Diagonalization of the quadratic boson Hamiltonian, Phys. A: Stat. Mech. Appl. **93**, 327 (1978).

[80] J. H. P. Colpa, Diagonalisation of the quadratic fermion Hamiltonian with a linear part, J. Phys. A: Math. Theor. **12**, 469 (1979).

[81] J. H. P. Colpa, Diagonalization of the quadratic boson Hamiltonian with zero modes: I. mathematical, Phys. A: Stat. Mech. Appl. **134**, 377 (1986).

[82] J. H. P. Colpa, Diagonalization of the quadratic boson Hamiltonian with zero modes: II. physical, Phys. A: Stat. Mech. Appl. **134**, 417 (1986).

[83] B. A. Bernevig, T. L. Hughes, and S.-C. Zhang, Quantum spin Hall effect and topological phase transition in HgTe quantum wells, Science **314**, 1757 (2006).

[84] R. Basnet, A. Wegner, K. Pandey, S. Storment, and J. Hu, Highly sensitive spin-flop transition in antiferromagnetic van der Waals material MPS_3 (M = Ni and Mn), Phys. Rev. Mater. **5**, 064413 (2021).

[85] T. Holstein and H. Primakoff, Field dependence of the intrinsic domain magnetization of a ferromagnet, Phys. Rev. **58**, 1098 (1940).

[86] P.-O. Löwdin, A note on the quantum-mechanical perturbation theory, J. Chem. Phys. **19**, 1396 (1951).

[87] P.-O. Löwdin, Partitioning technique, perturbation theory, and rational approximations, Int. J. Quantum Chem. **21**, 69 (1982).

[88] L. Jin and Z. Song, Partitioning technique for discrete quantum systems, Phys. Rev. A **83**, 062118 (2011).

[89] J. R. Schrieffer and P. A. Wolff, Relation between the Anderson and Kondo Hamiltonians, Phys. Rev. **149**, 491 (1966).

[90] S. Bravyi, D. P. DiVincenzo, and D. Loss, Schrieffer-Wolff transformation for quantum many-body systems, Ann. Phys. **326**, 2793 (2011).

[91] Z. Zhou, L.-L. Wan, and Z.-F. Xu, Topological classification of excitations in quadratic bosonic systems, J. Phys. A: Math. Theor. **53**, 425203 (2020).

[92] L.-L. Wan, Z. Zhou, and Z.-F. Xu, Squeezing-induced topological gap opening on bosonic Bogoliubov excitations, Phys. Rev. A **103**, 013308 (2021).

[93] G. Massarelli, I. Khait, and A. Paramekanti, Krein-unitary Schrieffer-Wolff transformation and band touchings in bosonic Bogoliubov-de Gennes and other Krein-Hermitian Hamiltonians, Phys. Rev. B **106**, 144434 (2022).

[94] T. Ohashi, S. Kobayashi, and Y. Kawaguchi, Generalized Berry phase for a bosonic Bogoliubov system with exceptional points, Phys. Rev. A **101**, 013625 (2020).

Supplemental Material for:
Giant spin Nernst effect in a two-dimensional antiferromagnet due to magnetoelastic coupling-induced gaps and interband transitions between magnon-like bands

D.-Q. To,[1] C. Y. Ameyaw,[1] A. Suresh,[2] S. Bhatt,[2] M. J. H. Ku,[1,2] M. B. Jungfleisch,[2] J. Q. Xiao,[2] J. M. O. Zide,[1] B. K. Nikolić,[2,*] and M. F. Doty[1,†]

[1] *Department of Materials Science and Engineering, University of Delaware, Newark, DE 19716, USA*
[2] *Department of Physics and Astronomy, University of Delaware, Newark, DE 19716, USA*

S1. MAGNON-PHONON HAMILTONIAN OF FEPS$_3$ IN BOGOLIUBOV-DE GENNES FORM: EXACT DIAGONALIZATION AND PERTURBATION THEORY

A. Magnon Hamiltonian via Holstein-Primakoff transformation

To derive a second-quantization version of Eq. (2) in the main text in terms of bosonic operators creating and annihilating magnons, we employ standard Holstein-Primakoff transformation [1] which maps spin operators [Eq. (2) in the main text] residing on sublattice A or B of a two-dimensional antiferromagnet (2D AFM), to bosonic ones and with its square root of operators expanded into Taylor series and then truncated [2] to linear order

$$S_A^+ = \sqrt{2S}a_i \qquad S_A^- = \sqrt{2S}a_i^\dagger \qquad S_A^z = S - a_i^\dagger a_i, \tag{S1}$$

$$S_B^+ = \sqrt{2S}b_j^\dagger \qquad S_B^- = \sqrt{2S}b_j \qquad S_B^z = -S + b_j^\dagger b_j. \tag{S2}$$

Such truncation is valid as long as the temperature is low, $k_BT \ll J_{ij}$ where J_{ij} is the exchange coupling in Eq. (2) in the main text, and the number of magnons excited is sufficiently small [2]. Here a_i and b_j ($a_i^\dagger$ and $b_j^\dagger$) are operators annihilating (creating) magnon at site $i \in A$ or site $j \in B$, respectively. Using the Fourier transform of these operators

$$a_i = \frac{1}{\sqrt{N}}\sum_{\boldsymbol{k}} e^{i\boldsymbol{k}\cdot\boldsymbol{r}_{a_i}} a_{\boldsymbol{k},i}, \tag{S3}$$

$$a_i^\dagger = \frac{1}{\sqrt{N}}\sum_{\boldsymbol{k}} e^{-i\boldsymbol{k}\cdot\boldsymbol{r}_{a_i}} a_{\boldsymbol{k},i}^\dagger, \tag{S4}$$

$$b_i = \frac{1}{\sqrt{N}}\sum_{\boldsymbol{k}} e^{i\boldsymbol{k}\cdot\boldsymbol{r}_{b_i}} b_{\boldsymbol{k},i}, \tag{S5}$$

$$b_i^\dagger = \frac{1}{\sqrt{N}}\sum_{\boldsymbol{k}} e^{-i\boldsymbol{k}\cdot\boldsymbol{r}_{b_i}} b_{\boldsymbol{k},i}^\dagger, \tag{S6}$$

the Heisenberg Hamiltonian in Eq. (2) of the main text can be re-written in second-quantization form as

$$H_m = E_m^0 + H_m(\boldsymbol{k}). \tag{S7}$$

Here E_m^0 is k-independent energy which simply shifts the energy-momentum dispersion of magnons by a constant value and, hence, can be neglected. The k-dependent terms, containing operators which create and annihilate magnons in

* bnikolic@udel.edu
† doty@udel.edu

momentum $\hbar\boldsymbol{k}$, are collected into $H_m(\boldsymbol{k})$ which can be written compactly in a matrix-vector multiplication form as

$$H_m(\boldsymbol{k}) = -2S\sum_{\boldsymbol{k}} \begin{pmatrix} a^\dagger_{\boldsymbol{k},1} \\ a^\dagger_{\boldsymbol{k},2} \\ b^\dagger_{\boldsymbol{k},1} \\ b^\dagger_{\boldsymbol{k},2} \\ a_{-\boldsymbol{k},1} \\ a_{-\boldsymbol{k},2} \\ b_{-\boldsymbol{k},1} \\ b_{-\boldsymbol{k},2} \end{pmatrix}^T \begin{bmatrix} A_1(\boldsymbol{k}) & B^*(\boldsymbol{k}) & 0 & 0 & 0 & 0 & C(\boldsymbol{k}) & D(\boldsymbol{k}) \\ B(\boldsymbol{k}) & A_1(\boldsymbol{k}) & 0 & 0 & 0 & 0 & D(\boldsymbol{k}) & C^*(\boldsymbol{k}) \\ 0 & 0 & A_2(\boldsymbol{k}) & B(\boldsymbol{k}) & C^*(\boldsymbol{k}) & D(\boldsymbol{k}) & 0 & 0 \\ 0 & 0 & B^*(\boldsymbol{k}) & A_2(\boldsymbol{k}) & D(\boldsymbol{k}) & C(\boldsymbol{k}) & 0 & 0 \\ 0 & 0 & C(\boldsymbol{k}) & D(\boldsymbol{k}) & A_1(\boldsymbol{k}) & B^*(\boldsymbol{k}) & 0 & 0 \\ 0 & 0 & D(\boldsymbol{k}) & C^*(\boldsymbol{k}) & B(\boldsymbol{k}) & A_1(\boldsymbol{k}) & 0 & 0 \\ C^*(\boldsymbol{k}) & D(\boldsymbol{k}) & 0 & 0 & 0 & 0 & A_2(\boldsymbol{k}) & B(\boldsymbol{k}) \\ D(\boldsymbol{k}) & C(\boldsymbol{k}) & 0 & 0 & 0 & 0 & B^*(\boldsymbol{k}) & A_2(\boldsymbol{k}) \end{bmatrix} \begin{pmatrix} a_{\boldsymbol{k},1} \\ a_{\boldsymbol{k},2} \\ b_{\boldsymbol{k},1} \\ b_{\boldsymbol{k},2} \\ a^\dagger_{-\boldsymbol{k},1} \\ a^\dagger_{-\boldsymbol{k},2} \\ b^\dagger_{-\boldsymbol{k},1} \\ b^\dagger_{-\boldsymbol{k},2} \end{pmatrix}, \tag{S8}$$

with the matrix elements given by

$$A_1(\boldsymbol{k}) = 3J_3 - J_1 + \Delta + J_2\left[2 + e^{i\boldsymbol{k}\cdot\boldsymbol{\beta}_1} + e^{-i\boldsymbol{k}\cdot\boldsymbol{\beta}_1}\right] + \frac{g\mu_B}{2S}B_z, \tag{S9}$$

$$A_2(\boldsymbol{k}) = 3J_3 - J_1 + \Delta + J_2\left[2 + e^{i\boldsymbol{k}\cdot\boldsymbol{\beta}_1} + e^{-i\boldsymbol{k}\cdot\boldsymbol{\beta}_1}\right] - \frac{g\mu_B}{2S}B_z, \tag{S10}$$

$$B(\boldsymbol{k}) = J_1\left(e^{i\boldsymbol{k}\cdot\boldsymbol{\alpha}_2} + e^{i\boldsymbol{k}\cdot\boldsymbol{\alpha}_3}\right), \tag{S11}$$

$$C(\boldsymbol{k}) = -J_1 e^{-i\boldsymbol{k}\cdot\boldsymbol{\alpha}_1} - J_3\left(e^{-i\boldsymbol{k}\cdot\boldsymbol{\gamma}_1} + e^{i\boldsymbol{k}\cdot\boldsymbol{\gamma}_2} + e^{-i\boldsymbol{k}\cdot\boldsymbol{\gamma}_3}\right), \tag{S12}$$

$$D(\boldsymbol{k}) = -J_2\left[e^{i\boldsymbol{k}\cdot\boldsymbol{\beta}_2} + e^{-i\boldsymbol{k}\cdot\boldsymbol{\beta}_2} + e^{i\boldsymbol{k}\cdot\boldsymbol{\beta}_3} + e^{-i\boldsymbol{k}\cdot\boldsymbol{\beta}_3}\right]. \tag{S13}$$

The vectors $\boldsymbol{\alpha}_i$, $\boldsymbol{\beta}_i$ and $\boldsymbol{\gamma}_i$ $(i = 1, 2, 3)$—connecting the first, second and third nearest neighbor atoms, respectively (see Fig. 1 in the main text)—are given by

$$\boldsymbol{\alpha}_1 = a(0, -1, 0), \qquad \boldsymbol{\alpha}_2 = a\left(\frac{\sqrt{3}}{2}, \frac{1}{2}, 0\right), \qquad \boldsymbol{\alpha}_3 = a\left(\frac{-\sqrt{3}}{2}, \frac{1}{2}, 0\right), \tag{S14}$$

$$\boldsymbol{\beta}_1 = a\left(\sqrt{3}, 0, 0\right), \qquad \boldsymbol{\beta}_2 = a\left(\frac{\sqrt{3}}{2}, -\frac{3}{2}, 0\right), \qquad \boldsymbol{\beta}_3 = a\left(\frac{\sqrt{3}}{2}, \frac{3}{2}, 0\right), \tag{S15}$$

$$\boldsymbol{\gamma}_1 = a\left(0, 2, 0\right), \qquad \boldsymbol{\gamma}_2 = a\left(\sqrt{3}, 1, 0\right) \qquad \boldsymbol{\gamma}_3 = a\left(\sqrt{3}, -1, 0\right), \tag{S16}$$

where a is the lattice spacing.

B. Phonon Hamiltonian

Using the Fourier transform of the momentum operator along the z-axis perpendicular to the plane of 2D AFM

$$p_i^z = \frac{1}{\sqrt{N}}\sum_{\boldsymbol{k}} p_{\boldsymbol{k}}^z e^{i\boldsymbol{k}\cdot\boldsymbol{r}_i}, \tag{S17}$$

and of the lattice displacement operator

$$u_i^z = \frac{1}{\sqrt{N}}\sum_{\boldsymbol{k}} u_{\boldsymbol{k}}^z e^{-i\boldsymbol{k}\cdot\boldsymbol{r}_i}, \tag{S18}$$

the Hamiltonian of out-of-plane lattice vibration [Eq. (3) in the main text] can be recast as

$$H_p = \sum_{\boldsymbol{k}} \frac{p_{\boldsymbol{k}}^z p_{-\boldsymbol{k}}^z}{2M} + \sum_{\boldsymbol{k}} \begin{pmatrix} u^z_{\boldsymbol{k},a_1} \\ u^z_{\boldsymbol{k},a_2} \\ u^z_{\boldsymbol{k},b_1} \\ u^z_{\boldsymbol{k},b_2} \end{pmatrix}^T \begin{bmatrix} E_1(\boldsymbol{k}) & E_2(\boldsymbol{k}) & E_3(\boldsymbol{k}) & E_4(\boldsymbol{k}) \\ c.c & E_1(\boldsymbol{k}) & E_4(\boldsymbol{k}) & E_3^*(\boldsymbol{k}) \\ c.c & c.c & E_1(\boldsymbol{k}) & E_2^*(\boldsymbol{k}) \\ c.c & c.c & c.c & E_1(\boldsymbol{k}), \end{bmatrix} \begin{pmatrix} u^z_{-\boldsymbol{k},a_1} \\ u^z_{-\boldsymbol{k},a_2} \\ u^z_{-\boldsymbol{k},b_1} \\ u^z_{-\boldsymbol{k},b_2} \end{pmatrix} \tag{S19}$$

where the elements of the dynamical matrix are given by

$$E_1(\boldsymbol{k}) = \zeta_0^z + \zeta_2^z\left(e^{i\boldsymbol{k}\cdot\boldsymbol{\beta}_1} + e^{-i\boldsymbol{k}\cdot\boldsymbol{\beta}_1}\right), \tag{S20}$$

$$E_2(\boldsymbol{k}) = \zeta_1^z\left(e^{-i\boldsymbol{k}\cdot\boldsymbol{\alpha}_2} + e^{-i\boldsymbol{k}\cdot\boldsymbol{\alpha}_3}\right), \tag{S21}$$

$$E_3(\boldsymbol{k}) = \zeta_1^z e^{-i\boldsymbol{k}\cdot\boldsymbol{\alpha}_1} + \zeta_3^z\left(e^{-i\boldsymbol{k}\cdot\boldsymbol{\gamma}_1} + e^{i\boldsymbol{k}\cdot\boldsymbol{\gamma}_2} + e^{-i\boldsymbol{k}\cdot\boldsymbol{\gamma}_3}\right), \tag{S22}$$

$$E_4(\boldsymbol{k}) = \zeta_2^z\left(e^{i\boldsymbol{k}\cdot\boldsymbol{\beta}_2} + e^{-i\boldsymbol{k}\cdot\boldsymbol{\beta}_2} + e^{i\boldsymbol{k}\cdot\boldsymbol{\beta}_3} + e^{-i\boldsymbol{k}\cdot\boldsymbol{\beta}_3}\right). \tag{S23}$$

Here $\zeta_0 = -3(\zeta_1+\zeta_3)-6\zeta_2$, with ζ_i^z $(i=1,2,3)$, are the spring constant of the first, second and third nearest neighbor atoms.

C. Magnetoelastic coupling Hamiltonian

Using Eqs. (S1)–(S6), the Hamiltonian of magnetoelastic coupling [Eq. (4) in the main text] can be recast as

$$H_{mp} = \sum_{\boldsymbol{k}} \begin{pmatrix} u^z_{\boldsymbol{k},a_1} \\ u^z_{\boldsymbol{k},a_2} \\ u^z_{\boldsymbol{k},b_1} \\ u^z_{\boldsymbol{k},b_2} \end{pmatrix}^T M(\boldsymbol{k}) \begin{pmatrix} a_{\boldsymbol{k},1} \\ a_{\boldsymbol{k},2} \\ b_{\boldsymbol{k},1} \\ b_{\boldsymbol{k},2} \\ a^\dagger_{-\boldsymbol{k},1} \\ a^\dagger_{-\boldsymbol{k},2} \\ b^\dagger_{-\boldsymbol{k},1} \\ b^\dagger_{-\boldsymbol{k},2} \end{pmatrix} + \text{H.c.}, \tag{S24}$$

where

$$M(\boldsymbol{k}) = \begin{bmatrix} 0 & -AC+\frac{BD}{2} & -Be^{-i\boldsymbol{k}\boldsymbol{\alpha}_1} & 0 & 0 & -AC-\frac{BD}{2} & Be^{-i\boldsymbol{k}\boldsymbol{\alpha}_1} & 0 \\ AC^*-\frac{BD^*}{2} & 0 & 0 & Be^{i\boldsymbol{k}\boldsymbol{\alpha}_1} & AC^*+\frac{BD^*}{2} & 0 & 0 & -Be^{i\boldsymbol{k}\boldsymbol{\alpha}_1} \\ Be^{i\boldsymbol{k}\boldsymbol{\alpha}_1} & 0 & 0 & -AC^*-\frac{BD^*}{2} & -Be^{i\boldsymbol{k}\boldsymbol{\alpha}_1} & 0 & 0 & -AC^*+\frac{BD^*}{2} \\ 0 & -Be^{-i\boldsymbol{k}\boldsymbol{\alpha}_1} & AC+\frac{BD}{2} & 0 & 0 & Be^{-i\boldsymbol{k}\boldsymbol{\alpha}_1} & AC-\frac{BD}{2} & 0 \end{bmatrix}, \tag{S25}$$

with

$$A = \frac{aS\sqrt{S}}{2\sqrt{6}}\xi, \qquad B = i\frac{aS\sqrt{S}}{3\sqrt{2}}\xi, \qquad C = e^{-i\boldsymbol{k}\cdot\boldsymbol{\alpha}_2} - e^{-i\boldsymbol{k}\cdot\boldsymbol{\alpha}_3}, \qquad D = e^{-i\boldsymbol{k}\cdot\boldsymbol{\alpha}_2} + e^{-i\boldsymbol{k}\cdot\boldsymbol{\alpha}_3}. \tag{S26}$$

Here, S is the spin value of Fe atom, ξ is the magnetoelastic (or magnon-phonon) coupling strength, and A^* denotes complex conjugate of A.

D. Hybridized magnon-phonon band structure of $FePS_3$ from exact diagonalization of BdG Hamiltonian

By adding [Eq. (1) in the main text] magnon [Eq. (S8)], phonon [Eq. (S19)] and magnetoelastic [Eq. (S20)] Hamiltonians, we then can construct the total Hamiltonian of magnon and phonons, including their hybridization, in 2D AFM $FePS_3$. With additional transformations, this Hamiltonian can be recast as bosonic Bogoliubov-de Gennes (BdG) Hamiltonian [3, 4]

$$H = \sum_{\boldsymbol{k}} \Psi^\dagger H(\boldsymbol{k})\Psi \tag{S27}$$

where $\Psi^\dagger = [x^\dagger_{\boldsymbol{k},1}, x^\dagger_{\boldsymbol{k},2}, ..., x^\dagger_{\boldsymbol{k},n}, x_{-\boldsymbol{k},1}, x_{-\boldsymbol{k},2}, ..., x_{-\boldsymbol{k},n}]$ is the Nambu spinor. By using Colpa's method [5], we diagonalize this Hamiltonian to obtain the eigenenergies of the system $E(\boldsymbol{k})$ satisfying the following eigenvalue equation

$$\boldsymbol{\sigma}_3 H(\boldsymbol{k})T(\boldsymbol{k}) = T(\boldsymbol{k})\boldsymbol{\sigma}_3 E(\boldsymbol{k}), \tag{S28}$$

as the generalized eigenvalue problem in which $\boldsymbol{\sigma}_3 H(\boldsymbol{k})$ is a non-Hermitian matrix even though $H(\boldsymbol{k})$ is Hermitian [6]. In other words, the diagonalization of the BdG Hamiltonian deals with non-Hermitian quantum mechanics [3, 4], but the eigenvalues $E(\boldsymbol{k})$ remain real. In Eq. (S28), matrix $T(\boldsymbol{k})$

$$T^\dagger(\boldsymbol{k})\boldsymbol{\sigma}_3 T(\boldsymbol{k}) = T(\boldsymbol{k})\boldsymbol{\sigma}_3 T^\dagger(\boldsymbol{k}) = \boldsymbol{\sigma}_3, \tag{S29}$$

is "paraunitiary", and $\boldsymbol{\sigma}_3$ matrix is given in Eq. (16) of the main text.

Table I lists the exchange couplings between localized spins used in Eq. (2) of the main text, spring constants used in Eq. (3) of the main text, and magnon-phonon coupling strength used in Eq. (4) of the main text. Using those parameters, Fig. S1(a) plots independent magnon and phonon bands of $FePS_3$ computed without applied magnetic field or magnetoelastic coupling—since $B_z = 0$, the magnon band is doubly-degenerate. The out of plane vibrational

Table I. The exchange coupling between localized spins, spring constants, and magnon-phonon coupling strengths for 2D AFM $FePS_3$.

Materials	a (Å)	S	J_1 (meV)	J_2 (meV)	J_3 (meV)	J′ (meV)	Δ (meV)	ζ_1 (meV/Å^2)	ζ_2 (meV/Å^2)	ζ_3 (meV/Å^2)	M	ξ (meV/Å)
$FePS_3$ [7, 8]	3.5	2	1.49	0.04	-0.6	-0.0073	-3.6	-129.9	-76.88	-0.769	5.6	0.95

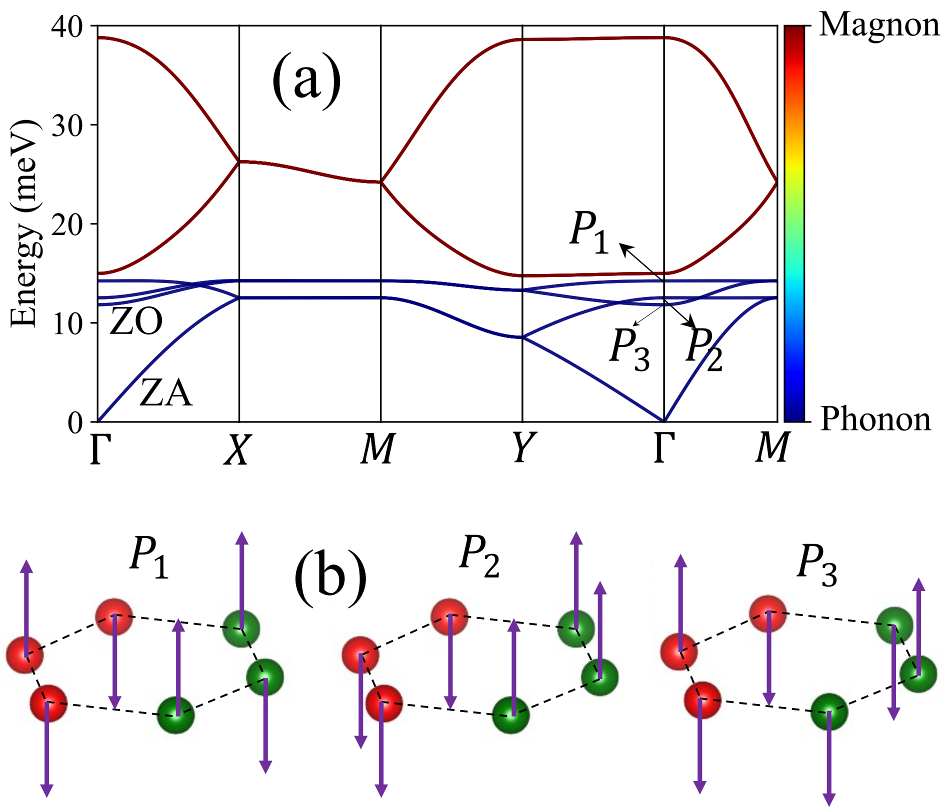

Figure S1. (a) The independent magnon and phonon band of $FePS_3$ along Γ-X-M-Y-Γ-M high symmetry path in the BZ calculated in the *absence* of both the applied magnetic field and magnon-phonon coupling. (b) Schematic of lattice vibrations at the Γ point associating with three modes P_1, P_2 and P_3. The arrows indicate the direction of motion of corresponding Fe atoms.

modes, i.e., phonons as the quanta of vibrational energy, include both acoustic and optical branches. By looking at the eigenvector of the phonon bands at the Γ point, we can specify three optical phonon modes P_i $(i = 1, 2, 3)$, as denoted in the Fig. S1(b).

Figure S2(a) also shows independent magnon and phonon bands computed in the absence of magnetoelastic coupling, but with applied magnetic field switched on and along $\bar{X}$-Γ-X path. Figure S2(a) highlights crossing of magnon and phonon bands (near Γ point), as well as between two magnon-like bands with zoom on their crossing provided in the inset. Once the magnetoelastic coupling is switched on, the magnon and phonon bands hybridize, while all of their crossings are lifted to become anticrossings in Fig. S2(b). The small anticrossing gap emerges between two magnon-like bands [inset of Fig. S2(b)], which leads to a finite Berry curvature of the 2nd and 3rd bands, as discussed in Sec. IIIA in the main text.

Figure S3 plots 1st and 2nd magnon-like bands calculated without an applied magnetic field, while zooming in on the region in the vicinity of the Γ point. In the absence of the magnetoelastic, Fig. S3(a) is the zoomed version of Fig. S2(a) but without applied magnetic field, showing clearly that magnon bands are degenerate in energy. When the magnetoelastic coupling is switched on [Fig. S3(b)], this degeneracy is lifter so that the same bands acquire slight energy splitting. Futhermore, the energy gap that opens between two magnon-like bands possessing opposite spin [Fig. S2(b)] as the consequence of the influence of perturbations from phonons onto magnon bands, as discussed using Eq. (18) in the main text, whose complete derivation is provided in Sec. S1 E.

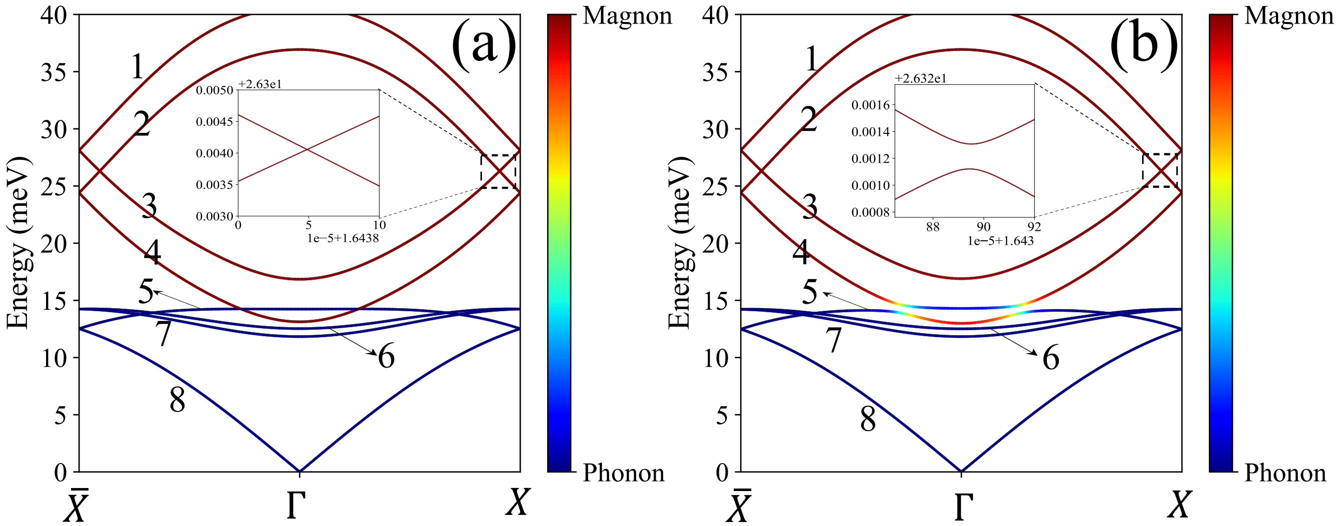

Figure S2. The magnon phonon dispersion in $FePS_3$ along the $\bar{X}$-Γ-X high symmetry path in the BZ calculated in applied magnetic field $B_z = 30$ T and with magnetoelastic coupling [Eq. (S20)] (a) switched off or (b) switched on. The inset in panel (b) shows the tiny gap between two magnon-like bands (2nd band and 3rd band) that is a result of magnetoelastic coupling, while in the inset of panel (a) these two bands cross each other because magnetoelastic is switched off. We note that in panel (b) the gap between 2nd and 3rd magnon-like band is very small in comparison to the hybridized gap near the Γ point between magnon and phonon bands (4th and 5th band).

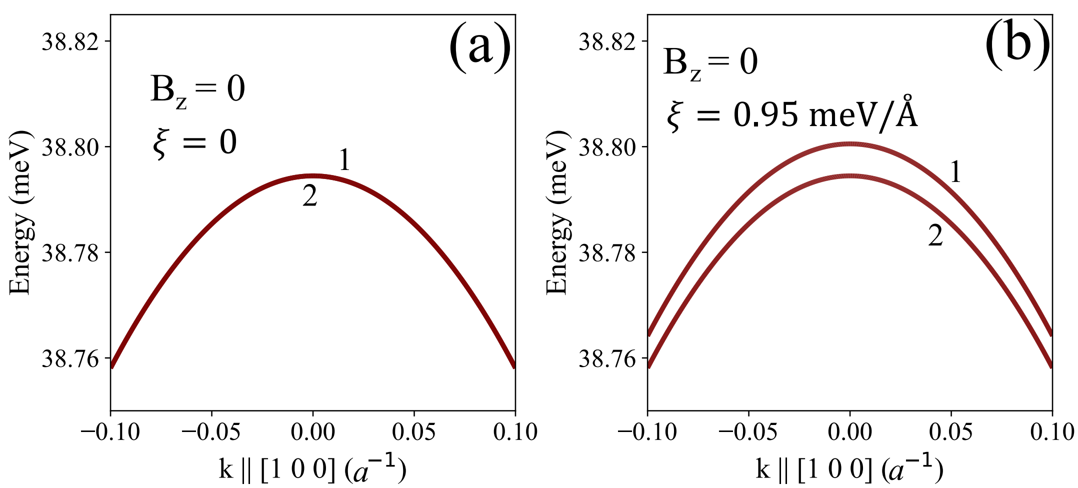

Figure S3. The 1st and 2nd magnon-like bands. marked in Fig. S2, calculated without the applied magnetic field ($B_z = 0$) and: (a) without the magnetoelastic coupling [$\xi = 0$ in Eqs. (S24)–(S26)]; or (b) with finite magnetoelastic coupling [$\xi \neq 0$ in Eqs. (S24)–(S26)].

E. Löwdin partitioning of BdG Hamiltonian

In order to elucidate the splitting between the first and second magnon-like bands due to perturbations from phonons [Fig S3(b)], we apply the Löwdin partitioning [9, 10] approach to the BdG Hamiltonian [Eq. (S27)]. A key concept in Löwdin partitioning, which is also known as the Schrieffer-Wolff transformation [11–16], is investigation of the effect of a perturbation on a subset of contiguous energy states of a Hermitian Hamiltonian [9]. Because the diagonalization of our bosonic BdG Hamiltonian requires to diagonalize a non-Hermitian Hamiltonian, in the following we discuss the Krein-Hermitian [16] and related properties of BdG Hamiltonian and then adapt the Löwdin partitioning to this case.

From Eq. (S29), we can obtain

$$T^{\dagger}(\boldsymbol{k}) = \boldsymbol{\sigma}_3^{-1} T^{-1}(\boldsymbol{k}) \boldsymbol{\sigma}_3 = \boldsymbol{\sigma}_3 T^{-1}(\boldsymbol{k}) \boldsymbol{\sigma}_3, \tag{S30}$$

where we use property $\boldsymbol{\sigma}_3^{-1} = \boldsymbol{\sigma}_3$. The congruence transformation of the magnon-phonon Hamiltonian can then be rewritten in terms of the following transformation

$$T(\boldsymbol{k})^{\dagger} H(\boldsymbol{k}) T(\boldsymbol{k}) = \boldsymbol{\sigma}_3 \left\{ T^{-1}(\boldsymbol{k}) \left[\boldsymbol{\sigma}_3 H(\boldsymbol{k}) \right] T(\boldsymbol{k}) \right\}, \tag{S31}$$

of a non-Hermitian matrix $\boldsymbol{\sigma}_3 H(\boldsymbol{k})$. The matrix $\boldsymbol{\sigma}_3 H(\boldsymbol{k})$ and the paraunitary matrix $T(\boldsymbol{k})$ are Krein-Hermitian and Krein-unitary, respectively, with respect to the $\boldsymbol{\sigma}_3$ [13]. If we define

$$\bar{H} = \boldsymbol{\sigma}_3 H(\boldsymbol{k}), \tag{S32}$$

together with a Krein-adjoint of matrix $T(\boldsymbol{k})$ as

$$T^{\#}(\boldsymbol{k}) = \boldsymbol{\sigma}_3^{-1} T^{\dagger}(\boldsymbol{k}) \boldsymbol{\sigma}_3 = \boldsymbol{\sigma}_3 T^{\dagger}(\boldsymbol{k}) \boldsymbol{\sigma}_3, \tag{S33}$$

then we find their following properties

$$T^{\#}(\boldsymbol{k}) T(\boldsymbol{k}) = T(\boldsymbol{k}) T^{\#}(\boldsymbol{k}) = \mathcal{I}, \tag{S34}$$

and

$$\bar{H} T(\boldsymbol{k}) = T(\boldsymbol{k}) \bar{E}(\boldsymbol{k}), \tag{S35}$$

where $\bar{E}(\boldsymbol{k}) = \boldsymbol{\sigma}_3 E(\boldsymbol{k})$ and $\mathcal{I}$ is the identity matrix. Equations (S34) and (S35) provide an eigenbasis for bosons analogous to the case of a fermionic system. We can, therefore, adapt the Löwdin partitioning to the Hamiltonian $\bar{H}$, from which we obtain the spectrum of $H(\boldsymbol{k})$ order by order in its perturbation. In the spirit of Löwdin partitioning, we decompose $\bar{H}$ as

$$\bar{H} = \bar{H}^0 + \bar{H}' \tag{S36}$$

where $\bar{H}^0$ is the zeroth order diagonal matrix, and $\bar{H}^{'}$ is the first order perturbation that can also be decomposed into two terms—$\bar{H}^{'} = \bar{H}^1 + \bar{H}^2$ with $\bar{H}^1$ being block-diagonal and composed of two submatrices while $\bar{H}^2$ is composed of off-diagonal submatrices, as illustrated visually in Fig. S4.

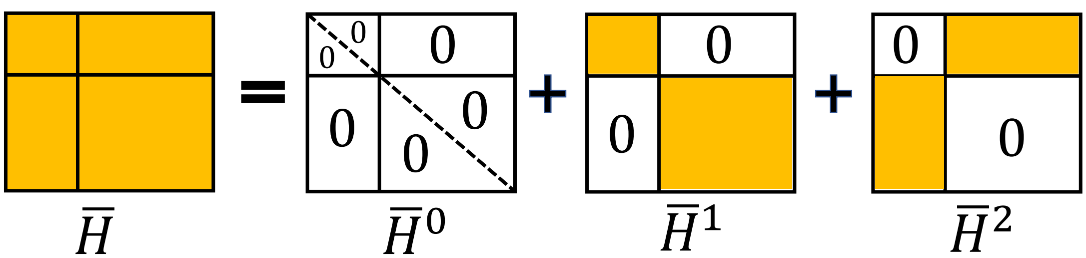

Figure S4. Visualization of the submatrix (or block) structure of the matrix representation of Hamiltonian $\bar{H}$ [Eq. (S32)] as a sum of $\bar{H}^0$, $\bar{H}^1$ and $\bar{H}^2$, where $\bar{H}^0$ is truly diagonal; $\bar{H}^1$ is a block-diagonal; and $\bar{H}^2$ is a block off-diagonal matrix.

Our strategy is to find a matrix W that block-diagonalizes $\bar{H}$ with the Schrieffer-Wolff transformation:

$$\widetilde{\bar{H}} = e^{-W} \bar{H} e^{W} = \bar{H} + \left[\bar{H}, W \right] + \frac{1}{2} \left[\left[\bar{H}, W \right], W \right] + ..., \tag{S37}$$

Here e^{W} is a paraunitary matrix and W is a block off-diagonal matrix like $\bar{H}^2$. One can see that we must construct a matrix W such that the transformation in Eq. (S37) converts $\bar{H}^2$ into a block diagonal matrix like $\bar{H}^1$. Moreover, because e^{W} is Krein-unitary, W must be skew-Krein-unitary, i.e., $W = -\boldsymbol{\sigma}_3^{-1} W^{\dagger} \boldsymbol{\sigma}_3 = -\boldsymbol{\sigma}_3 W^{\dagger} \boldsymbol{\sigma}_3$. To determine W, we define $W = W^{(1)} + W^{(2)} + ...$ where $W^{(i)}$ is the ith order perturbation of W. The matrix W is then evaluated recursively order by order

$$\left[\bar{H}^0, W^{(1)} \right] = -\bar{H}^2, \tag{S38}$$

$$\left[\bar{H}^0, W^{(2)} \right] = -\left[\bar{H}^1, W^{(1)} \right], \tag{S39}$$

$$\left[\bar{H}^0, W^{(3)} \right] = -\left[\bar{H}^1, W^{(2)} \right] - \frac{1}{3} \left[\left[\bar{H}^2, W^{(1)} \right], W^{(1)} \right], \tag{S40}$$

$$... = ... \tag{S41}$$

The eigenbasis $T^0(\boldsymbol{k})$ and its Krein-adjoint $T^{0\#}(\boldsymbol{k})$ of $\bar{H}^0$ defined matrix representation of $\bar{H}^0$ which is a diagonal matrix satisfying

$$\bar{H}^0 T^0(\boldsymbol{k}) = T^0(\boldsymbol{k})\bar{E}^0(\boldsymbol{k}). \tag{S42}$$

Here $T^0(\boldsymbol{k})$ obeys

$$T^{0\#}(\boldsymbol{k})T^0(\boldsymbol{k}) = T^0(\boldsymbol{k})T^{0\#}(\boldsymbol{k}) = \mathcal{I}, \tag{S43}$$

leading to

$$T^{0\#}(\boldsymbol{k})\bar{H}^0 T^0(\boldsymbol{k}) = \bar{E}^0(\boldsymbol{k}). \tag{S44}$$

We then solve, for instance, Eq. (S38) by multiplying its both sides—by $T^{0\#}(\boldsymbol{k})$ from the left and by $T^0(\boldsymbol{k})$ from the right—to arrive at

$$T^{0\#}(\boldsymbol{k})\left[\bar{H}^0, W^{(1)}\right]T^0(\boldsymbol{k}) = -T^{0\#}(\boldsymbol{k})\bar{H}^2 T^0(\boldsymbol{k}), \tag{S45}$$

$$\Rightarrow T^{0\#}(\boldsymbol{k})\bar{H}^0 W^{(1)} T^0(\boldsymbol{k}) - T^{0\#}(\boldsymbol{k})W^{(1)}\bar{H}^0 T^0(\boldsymbol{k}) = -T^{0\#}(\boldsymbol{k})\bar{H}^2 T^0(\boldsymbol{k}). \tag{S46}$$

Using Eq. (S43) then leads to

$$T^{0\#}(\boldsymbol{k})\bar{H}^0 T^0(\boldsymbol{k})T^{0\#}(\boldsymbol{k})W^{(1)}T^0(\boldsymbol{k}) - T^{0\#}(\boldsymbol{k})W^{(1)}T^0(\boldsymbol{k})T^{0\#}(\boldsymbol{k})\bar{H}^0 T^0(\boldsymbol{k}) = -T^{0\#}(\boldsymbol{k})\bar{H}^2 T^0(\boldsymbol{k}), \tag{S47}$$

making it possible to write

$$\bar{E}^0(\boldsymbol{k})\left[W^{(1)}\right] - \left[W^{(1)}\right]\bar{E}^0(\boldsymbol{k}) = -\left[\bar{H}^2\right], \tag{S48}$$

where $[\mathcal{M}] = T^{0\#}(\boldsymbol{k})\mathcal{M}T^0(\boldsymbol{k})$. Since $\bar{E}^0(\boldsymbol{k})$ is a diagonal matrix, the diagonal terms of $\left[W^{(1)}\right]$ vanish, i.e., $\left[W^{(1)}\right]_{nn} = 0$. The off-diagonal terms of $\left[W^{(1)}\right]$ obtained from Eq. (S48) are then given by

$$\left[W^{(1)}\right]_{mn} = -\frac{\left[\bar{H}^2\right]_{mn}}{\bar{E}^0_m(\boldsymbol{k}) - \bar{E}^0_n(\boldsymbol{k})}, \tag{S49}$$

where $\bar{E}^0_i(\boldsymbol{k})$ is the ith eigenvalue of $\bar{H}^0$. By repeating the same procedure one can generate expressions for higher orders of W

$$\left[W^{(2)}\right]_{mn} = \frac{1}{\bar{E}^0_m(\boldsymbol{k}) - \bar{E}^0_n(\boldsymbol{k})}\left(\sum_{m'}\frac{\left[\bar{H}^2\right]_{mm'}\left[\bar{H}^1\right]_{m'n}}{\bar{E}^0_{m'}(\boldsymbol{k}) - \bar{E}^0_n(\boldsymbol{k})} - \sum_{n'}\frac{\left[\bar{H}^1\right]_{mn'}\left[\bar{H}^2\right]_{n'n}}{\bar{E}^0_m(\boldsymbol{k}) - \bar{E}^0_{n'}(\boldsymbol{k})}\right), \tag{S50}$$

$$... = ... \tag{S51}$$

Using Eqs. (S37), (S38), (S39) and (S40), we then obtain up to the second order

$$\widetilde{H} \approx \bar{H}^0 + \bar{H}^1 + \frac{1}{2}\left[\bar{H}^2, W^{(1)} + W^{(2)}\right]. \tag{S52}$$

The matrix elements of $\widetilde{H}$ in the eigenbasis of $\bar{H}^0$ can thus be expressed order by order as follows

$$\widetilde{H}^{(0)}_{nn'} = \left[\bar{H}^0\right]_{nn'}, \tag{S53}$$

$$\widetilde{H}^{(1)}_{nn'} = \left[\bar{H}^1\right]_{nn'}, \tag{S54}$$

$$\widetilde{H}^{(2)}_{nn'} = \frac{1}{2}\sum_m \left[\bar{H}^2\right]_{nm}\left[\bar{H}^2\right]_{mn'}\left(\frac{1}{\bar{E}^0_n(\boldsymbol{k}) - \bar{E}^0_m(\boldsymbol{k})} + \frac{1}{\bar{E}^0_{n'}(\boldsymbol{k}) - \bar{E}^0_m(\boldsymbol{k})}\right). \tag{S55}$$

Finally, we can describe the energy gap opening [inset of Fig. S2(b)] between the 1st and 2nd magnon bands due to the perturbations from phonons in the 2D AFM $FePS_3$ without an applied magnetic field ($B_z = 0$). For this purpose we suppose the magnetoelastic coupling Hamiltonian H_{mp} [Eq. (S24)] plays the role of a perturbation for the Hamiltonian of independent magnons and phonons, $H_m + H_p$ [i.e., the sum of Eqs. (S8) and (S19)]. We then apply the Löwdin partitioning to $\bar{H}^0 = H_m + H_p$ while using $\bar{H}^{'} \equiv H_{mp}$, to arrive at 2×2 effective Hamiltonian describing the first two magnon bands under the perturbation by magnetoelastic coupling. Because H_{mp} does not couple the two magnon states, such 2×2 effective Hamiltonian describing the first two magnon bands obtained from the Löwdin partitioning can be expressed as

$$\widetilde{H}_{2\times 2} = \bar{H}^0_{2\times 2} + \bar{H}^2_{2\times 2}, \tag{S56}$$

where

$$\bar{H}^0_{2\times 2} = \begin{pmatrix} \bar{E}_1(\boldsymbol{k}) & 0 \\ 0 & \bar{E}_2(\boldsymbol{k}) \end{pmatrix}, \tag{S57}$$

and

$$\bar{H}^2_{2\times 2} = \begin{pmatrix} h_{11} & h_{12} \\ h_{21} & h_{22} \end{pmatrix}. \tag{S58}$$

Here $\bar{E}_1(\boldsymbol{k}) = \bar{E}_2(\boldsymbol{k})$ are the non-perturbed energy-momentum dispersion of the 1st and 2nd magnon bands, which are degenerate [Fig. S3(a)] in the absence of magnetoelastic coupling and applied magnetic field. The matrix elements of $\bar{H}^2_{2\times 2}$ are given by

$$h_{mn} = \frac{1}{2}\sum_l \left[\bar{H}^2\right]_{ml}\left[\bar{H}^2\right]_{ln}\left(\frac{1}{\bar{E}^0_m(\boldsymbol{k}) - \bar{E}^0_l(\boldsymbol{k})} + \frac{1}{\bar{E}^0_n(\boldsymbol{k}) - \bar{E}^0_l(\boldsymbol{k})}\right). \tag{S59}$$

Using the Maclaurin series, $e^x = \sum_0^\infty \frac{x^n}{n!} = 1 + x + \frac{x^2}{2} + ...$, in the limit $x \ll 1$, so that $e^x \approx 1 + x$, Eq. (S25) for magnetoelastic coupling in the vicinity of the Γ-point is found to be linear in the wavevector $\boldsymbol{k}$. In other words, $\left[\bar{H}^2\right]_{ml}$ is linear in $\boldsymbol{k}$, thereby leading to h_{mn} which is quadratic in the wavevector $\boldsymbol{k}$. Because h_{mn} determines the energy splitting between the 1st and 2nd magnon-like bands, the energy gap between them due to magnon-phonon coupling is quadratic in the wavevector $\boldsymbol{k}$ near the Γ-point. Using the same argument, when the wave vector $\boldsymbol{k}$ becomes comparable to $\sim a^{-1}$ then the higher order terms, specifically the second order in $\boldsymbol{k}$, would contribute to the magnetoelastic coupling and the energy gap will acquire quartic dependence on wavevector $\boldsymbol{k}$.

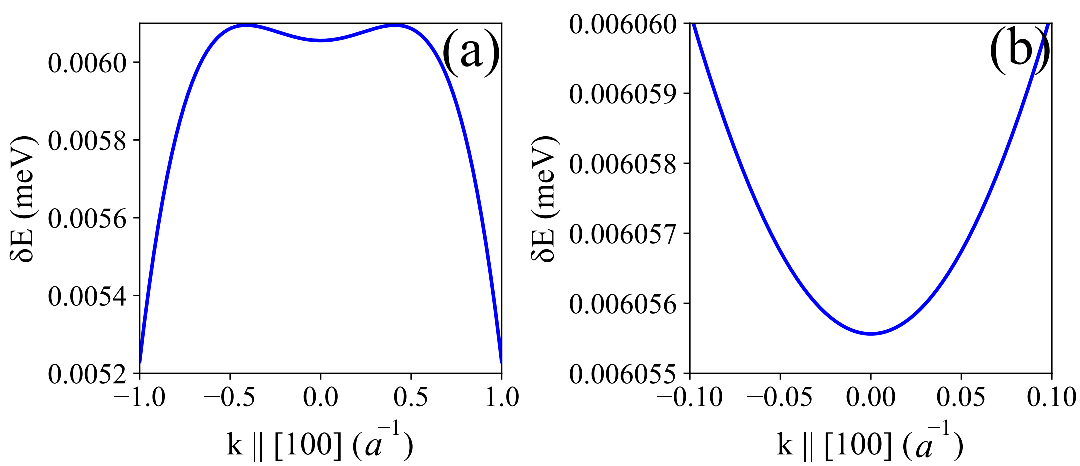

Figure S5. The energy splitting [Fig. S3(b)] between the 1st and 2nd magnon-like bands along [100] direction induced by magnetoelastic coupling in the absence of applied magnetic field ($B_z = 0$).

Figure S5 plot the energy splitting δE between the 1st and 2nd magnon bands [Fig. S3(b)] as a function of wavevector $\boldsymbol{k}$ along the [100] direction calculated from the total effective magnon-phonon Hamiltonian (with 16×16 bands), $H_m + H_p + H_{mp}$. When the wavevector varies over a wide range, the δE behaves like a quartic function [Fig. S5(a)]. As shown in Fig. S5(b), when the wavevector is small, typically in a range between $\pm 0.1\ a^{-1}$, we observe the expected quadratic (parabolic) dependence of δE on $\boldsymbol{k}$. This analysis fully explains the origin of the gap opening between the two magnon-like bands carrying opposite spin [Fig. S3(b)] as the consequence of perturbations from phonons, despite these two bands being distant in energy from manifestly hybridized magnon-phonon bands [around 15 meV in Fig. S2(b)] and their anticrossings near the Γ-point. Such gap opening between the magnon-like bands makes possible interband transition inducing spin-Berry curvature, which is very large due to the smallness of the gap, as discussed in the main text and elaborated further in Sec. S2.

S2. BERRY AND SPIN BERRY CURVATURE OF HYBRIDIZED MAGNON-PHONON BANDS

A. Berry curvature

In this Section, we provide detailed derivation of Eq. (13) in the main text for the Berry curvature of magnon-phonon bands. Starting from the Berry curvature formula for the BdG Hamiltonian [3, 4]

$$\Omega_n^z(\boldsymbol{k}) = i\epsilon_{xy}\left[\boldsymbol{\sigma}_3\frac{\partial T^\dagger(\boldsymbol{k})}{\partial k_x}\boldsymbol{\sigma}_3\frac{\partial T(\boldsymbol{k})}{\partial k_y}\right]_{nn}, \tag{S60}$$

we obtain

$$\begin{aligned}\Omega_n^z(\boldsymbol{k}) &= i\sum_m\left[\boldsymbol{\sigma}_3\frac{\partial T^\dagger(\boldsymbol{k})}{\partial k_x}\right]_{nm}\left[\boldsymbol{\sigma}_3\frac{\partial T(\boldsymbol{k})}{\partial k_y}\right]_{mn} - i\sum_m\left[\boldsymbol{\sigma}_3\frac{\partial T^\dagger(\boldsymbol{k})}{\partial k_y}\right]_{nm}\left[\boldsymbol{\sigma}_3\frac{\partial T(\boldsymbol{k})}{\partial k_x}\right]_{mn}\\ &= i\sum_m\sigma_3^{nn}\frac{\partial\left[T^\dagger(\boldsymbol{k})\right]_{nm}}{\partial k_x}\sigma_3^{mm}\frac{\partial\left[T(\boldsymbol{k})\right]_{mn}}{\partial k_y} - i\sum_m\sigma_3^{nn}\frac{\partial\left[T^\dagger(\boldsymbol{k})\right]_{nm}}{\partial k_y}\sigma_3^{mm}\frac{\partial\left[T(\boldsymbol{k})\right]_{mn}}{\partial k_x}.\end{aligned} \tag{S61}$$

By defining $|n(\boldsymbol{k})\rangle_m = [T(\boldsymbol{k})]_{mn}$ as the mth element of a column vector $|n(\boldsymbol{k})\rangle$, so that $\langle n(\boldsymbol{k})|_m = \left[T^\dagger(\boldsymbol{k})\right]_{nm}$ is the mth element of a row vector $\langle n(\boldsymbol{k})|$, Eq. (S34) can be rewritten as

$$\sum_n\sigma_3^{nn}|n(\boldsymbol{k})\rangle\boldsymbol{\sigma}_3\langle n(\boldsymbol{k})| = \sum_n\sigma_3^{nn}|n(\boldsymbol{k})\rangle\langle n(\boldsymbol{k})|\boldsymbol{\sigma}_3 = \mathcal{I}, \tag{S62}$$

which is the completeness relation for the BdG Hamiltonian eigenbasis. Using Eq. (S62), we can rewrite Eq. (S61) as

$$\begin{aligned}\Omega_n^z(\boldsymbol{k}) &= i\sum_m\sigma_3^{nn}\frac{\partial\langle n(\boldsymbol{k})|_m}{\partial k_x}\sigma_3^{mm}\frac{\partial|n(\boldsymbol{k})\rangle_m}{\partial k_y} - i\sum_m\sigma_3^{nn}\frac{\partial\langle n(\boldsymbol{k})|_m}{\partial k_y}\sigma_3^{mm}\frac{\partial|n(\boldsymbol{k})\rangle_m}{\partial k_x}\\ &= i\sigma_3^{nn}\left\langle\frac{\partial n(\boldsymbol{k})}{\partial k_x}\right|\boldsymbol{\sigma}_3\left|\frac{\partial n(\boldsymbol{k})}{\partial k_y}\right\rangle - i\sigma_3^{nn}\left\langle\frac{\partial n(\boldsymbol{k})}{\partial k_y}\right|\boldsymbol{\sigma}_3\left|\frac{\partial n(\boldsymbol{k})}{\partial k_x}\right\rangle\\ &= i\sum_{m\neq n}\sigma_3^{nn}\sigma_3^{mm}\left\langle\frac{\partial n(\boldsymbol{k})}{\partial k_x}\right|\boldsymbol{\sigma}_3\left|m(\boldsymbol{k})\right\rangle\left\langle m(\boldsymbol{k})\right|\boldsymbol{\sigma}_3\left|\frac{\partial n(\boldsymbol{k})}{\partial k_y}\right\rangle - i\sum_{m\neq n}\sigma_3^{nn}\sigma_3^{mm}\left\langle\frac{\partial n(\boldsymbol{k})}{\partial k_y}\right|\boldsymbol{\sigma}_3\left|m(\boldsymbol{k})\right\rangle\left\langle m(\boldsymbol{k})\right|\boldsymbol{\sigma}_3\left|\frac{\partial n(\boldsymbol{k})}{\partial k_x}\right\rangle,\end{aligned} \tag{S63}$$

leading to

$$\Omega_n^z(\boldsymbol{k}) = i\sum_{m\neq n}\sigma_3^{nn}\sigma_3^{mm}\left\langle\frac{\partial n(\boldsymbol{k})}{\partial k_x}\right|\boldsymbol{\sigma}_3\left|m(\boldsymbol{k})\right\rangle\left\langle m(\boldsymbol{k})\right|\boldsymbol{\sigma}_3\left|\frac{\partial n(\boldsymbol{k})}{\partial k_y}\right\rangle - (k_x\longleftrightarrow k_y). \tag{S64}$$

By taking the derivative of both sides of Eq. (S28) with respect to k_x, and by using $\langle n(\boldsymbol{k})| = \left[T^\dagger(\boldsymbol{k})\right]_{n\cdots}$ (the nth row of $\left[T^\dagger(\boldsymbol{k})\right]$ matrix) and $|n(\boldsymbol{k})\rangle = [T(\boldsymbol{k})]_{\cdots n}$ (the nth column of $[T(\boldsymbol{k})]$ matrix) we obtain

$$\boldsymbol{\sigma}_3\frac{\partial H(\boldsymbol{k})}{\partial k_x}|n(\boldsymbol{k})\rangle + \boldsymbol{\sigma}_3H(\boldsymbol{k})\left|\frac{\partial n(\boldsymbol{k})}{\partial k_x}\right\rangle = \left[\boldsymbol{\sigma}_3\frac{\partial E(\boldsymbol{k})}{\partial k_x}\right]_{nn}|n(\boldsymbol{k})\rangle + [\boldsymbol{\sigma}_3E(\boldsymbol{k})]_{nn}\left|\frac{\partial n(\boldsymbol{k})}{\partial k_x}\right\rangle. \tag{S65}$$

Multiplying both sides of Eq. (S65) with $\langle m(\boldsymbol{k})|\boldsymbol{\sigma}_3$ gives

$$\left\langle m(\boldsymbol{k})\right|\frac{\partial H(\boldsymbol{k})}{\partial k_x}\left|n(\boldsymbol{k})\right\rangle + \left\langle m(\boldsymbol{k})\right|H(\boldsymbol{k})\left|\frac{\partial n(\boldsymbol{k})}{\partial k_x}\right\rangle = \left[\boldsymbol{\sigma}_3\frac{\partial E(\boldsymbol{k})}{\partial k_x}\right]_{nn}\langle m(\boldsymbol{k})|\boldsymbol{\sigma}_3|n(\boldsymbol{k})\rangle + [\boldsymbol{\sigma}_3E(\boldsymbol{k})]_{nn}\left\langle m(\boldsymbol{k})\right|\boldsymbol{\sigma}_3\left|\frac{\partial n(\boldsymbol{k})}{\partial k_x}\right\rangle. \tag{S66}$$

Note that

$$\langle m(\boldsymbol{k})|\boldsymbol{\sigma}_3|n(\boldsymbol{k})\rangle = 0, \tag{S67}$$

with $m\neq n$ and

$$\left\langle m(\boldsymbol{k})\right|H(\boldsymbol{k})\left|\frac{\partial n(\boldsymbol{k})}{\partial k_x}\right\rangle = [\boldsymbol{\sigma}_3E(\boldsymbol{k})]_{mm}\left\langle m(\boldsymbol{k})\right|\boldsymbol{\sigma}_3\left|\frac{\partial n(\boldsymbol{k})}{\partial k_x}\right\rangle. \tag{S68}$$

Therefore,

$$\left\langle m(\boldsymbol{k}) \left| \frac{\partial H(\boldsymbol{k})}{\partial k_x} \right| n(\boldsymbol{k}) \right\rangle = \{[\boldsymbol{\sigma}_3 E(\boldsymbol{k})]_{nn} - [\boldsymbol{\sigma}_3 E(\boldsymbol{k})]_{mm}\} \left\langle m(\boldsymbol{k}) \left| \boldsymbol{\sigma}_3 \right| \frac{\partial n(\boldsymbol{k})}{\partial k_x} \right\rangle , \tag{S69}$$

leads to

$$\frac{\left\langle m(\boldsymbol{k}) \left| \frac{\partial H(\boldsymbol{k})}{\partial k_x} \right| n(\boldsymbol{k}) \right\rangle}{[\boldsymbol{\sigma}_3 E(\boldsymbol{k})]_{nn} - [\boldsymbol{\sigma}_3 E(\boldsymbol{k})]_{mm}} = \left\langle m(\boldsymbol{k}) \left| \boldsymbol{\sigma}_3 \right| \frac{\partial n(\boldsymbol{k})}{\partial k_x} \right\rangle , \tag{S70}$$

and, similarly, we obtain

$$\frac{\left\langle n(\boldsymbol{k}) \left| \frac{\partial H(\boldsymbol{k})}{\partial k_x} \right| m(\boldsymbol{k}) \right\rangle}{[\boldsymbol{\sigma}_3 E(\boldsymbol{k})]_{nn} - [\boldsymbol{\sigma}_3 E(\boldsymbol{k})]_{mm}} = \left\langle \frac{\partial n(\boldsymbol{k})}{\partial k_x} \left| \boldsymbol{\sigma}_3 \right| m(\boldsymbol{k}) \right\rangle, \tag{S71}$$

$$\frac{\left\langle m(\boldsymbol{k}) \left| \frac{\partial H(\boldsymbol{k})}{\partial k_y} \right| n(\boldsymbol{k}) \right\rangle}{[\boldsymbol{\sigma}_3 E(\boldsymbol{k})]_{nn} - [\boldsymbol{\sigma}_3 E(\boldsymbol{k})]_{mm}} = \left\langle m(\boldsymbol{k}) \left| \boldsymbol{\sigma}_3 \right| \frac{\partial n(\boldsymbol{k})}{\partial k_y} \right\rangle , \tag{S72}$$

$$\frac{\left\langle n(\boldsymbol{k}) \left| \frac{\partial H(\boldsymbol{k})}{\partial k_y} \right| m(\boldsymbol{k}) \right\rangle}{[\boldsymbol{\sigma}_3 E(\boldsymbol{k})]_{nn} - [\boldsymbol{\sigma}_3 E(\boldsymbol{k})]_{mm}} = \left\langle \frac{\partial n(\boldsymbol{k})}{\partial k_y} \left| \boldsymbol{\sigma}_3 \right| m(\boldsymbol{k}) \right\rangle . \tag{S73}$$

Combining Eq. (S64) with Eqs. (S70)– (S73), we finally arrive at the expression for the Berry curvature

$$\begin{aligned} \Omega_n^z(\boldsymbol{k}) &= \sum_{m\neq n} i\sigma_3^{nn}\sigma_3^{mm} \frac{\left\langle n(\boldsymbol{k}) \left| \frac{\partial H(\boldsymbol{k})}{\partial k_x} \right| m(\boldsymbol{k}) \right\rangle \left\langle m(\boldsymbol{k}) \left| \frac{\partial H(\boldsymbol{k})}{\partial k_y} \right| n(\boldsymbol{k}) \right\rangle}{\{[\boldsymbol{\sigma}_3 E(\boldsymbol{k})]_{nn} - [\boldsymbol{\sigma}_3 E(\boldsymbol{k})]_{mm}\}^2} - (k_x \longleftrightarrow k_y) \\ &= \sum_{m\neq n} i\sigma_3^{nn}\sigma_3^{mm} \frac{\left\langle n(\boldsymbol{k}) \left| \frac{\partial H(\boldsymbol{k})}{\partial k_x} \right| m(\boldsymbol{k}) \right\rangle \left\langle m(\boldsymbol{k}) \left| \frac{\partial H(\boldsymbol{k})}{\partial k_y} \right| n(\boldsymbol{k}) \right\rangle}{[\sigma_3^{nn} E_n(\boldsymbol{k}) - \sigma_3^{mm} E_m(\boldsymbol{k})]^2} - (k_x \longleftrightarrow k_y) \end{aligned} \tag{S74}$$

which can also be generalized into

$$\boldsymbol{\Omega}_n(\boldsymbol{k}) = \sum_{m\neq n} \frac{i\hbar^2 \langle n(\boldsymbol{k})|\boldsymbol{v}|m(\boldsymbol{k})\rangle\langle m(\boldsymbol{k})|\boldsymbol{\sigma}_3|m(\boldsymbol{k})\rangle \times \langle m(\boldsymbol{k})|\boldsymbol{v}|n(\boldsymbol{k})\rangle\langle n(\boldsymbol{k})|\boldsymbol{\sigma}_3|n(\boldsymbol{k})\rangle}{[\sigma_3^{nn} E_n(\boldsymbol{k}) - \sigma_3^{mm} E_m(\boldsymbol{k})]^2}, \tag{S75}$$

thereby completing the derivation of Eq. (13) in the main text.

B. Symmetry constraints on Berry curvature

The two important symmetries constraining the value of the Berry curvature are effective parity-time ($\mathcal{PT}$) and time-reversal symmetry ($\mathcal{TRS}$). Under these two symmetries, either the Berry curvature of the magnon-polaron or its sum over the entire Brillouin zone (BZ) are forced to vanish. This, in turn, results in zero thermal Hall conductivity.

1. *Effective parity-time symmetry*

Suppose that the bosonic system we consider is invariant under the effective $\mathcal{PT}$ operation

$$[H(\boldsymbol{k}), \mathcal{PT}] = 0. \tag{S76}$$

Here $\mathcal{PT} = \mathcal{CK}$, where $\mathcal{C}$ is a paraunitary matrix obeying $\mathcal{C}^\dagger\boldsymbol{\sigma}_3\mathcal{C} = \mathcal{C}\boldsymbol{\sigma}_3\mathcal{C}^\dagger = \boldsymbol{\sigma}_3$ and $\mathcal{K}$ is the complex conjugate operator. The BdG Hamiltonian then satisfied the following relation

$$\mathcal{C}^\dagger H^*(\boldsymbol{k})\mathcal{C} = H(\boldsymbol{k}), \tag{S77}$$

Substituting Eq. (S77) into the eigenequation for the magnon-phonon Hamiltonian in Eq. (S28), we obtain

$$\boldsymbol{\sigma}_3\mathcal{C}^\dagger H^*(\boldsymbol{k})\mathcal{C}T(\boldsymbol{k}) = \boldsymbol{\sigma}_3 H(\boldsymbol{k})T(\boldsymbol{k}) = T(\boldsymbol{k})\boldsymbol{\sigma}_3 E(\boldsymbol{k}), \tag{S78}$$

$$\boldsymbol{\sigma}_3\mathcal{C}^\dagger H^*(\boldsymbol{k})\mathcal{C}T(\boldsymbol{k}) = T(\boldsymbol{k})\boldsymbol{\sigma}_3 E(\boldsymbol{k}). \tag{S79}$$

By multiplying both sides of Eq. (S79) by $\mathcal{C}$ from the left we obtain

$$\mathcal{C}\boldsymbol{\sigma}_3\mathcal{C}^\dagger H^*(\boldsymbol{k})\mathcal{C}T(\boldsymbol{k}) = \mathcal{C}T(\boldsymbol{k})\boldsymbol{\sigma}_3 E(\boldsymbol{k}), \tag{S80}$$

leading to

$$\boldsymbol{\sigma}_3 H^*(\boldsymbol{k})\mathcal{C}T(\boldsymbol{k}) = \mathcal{C}T(\boldsymbol{k})\boldsymbol{\sigma}_3 E(\boldsymbol{k}). \tag{S81}$$

Taking the complex conjugate of Eq. (S81) gives

$$\left[\boldsymbol{\sigma}_3 H^*(\boldsymbol{k})\mathcal{C}T(\boldsymbol{k})\right]^* = \left[\mathcal{C}T(\boldsymbol{k})\boldsymbol{\sigma}_3 E(\boldsymbol{k})\right]^*. \tag{S82}$$

Since both $\boldsymbol{\sigma}_3$ and $E(\boldsymbol{k})$ are composed of real numbers, we obtain

$$\boldsymbol{\sigma}_3 H(\boldsymbol{k})\mathcal{C}^*T^*(\boldsymbol{k}) = \mathcal{C}^*T^*(\boldsymbol{k})\boldsymbol{\sigma}_3 E(\boldsymbol{k}). \tag{S83}$$

One can see that $\mathcal{C}^*T^*(\boldsymbol{k})$ plays the same role as $T(\boldsymbol{k})$, i.e., it obeys the same eigenvalue equation as $T(\boldsymbol{k})$. This means that they differ only by a phase factor matrix, i.e., a diagonal matrix with phase factor entries. We can ignore this phase factor when considering the Berry curvature [4], therefore, allowing us to write

$$T(\boldsymbol{k}) = \mathcal{C}^*T^*(\boldsymbol{k}). \tag{S84}$$

Inserting Eq. (S84) into the expression for the Berry curvature written in terms of the paraunitary matrix $T(\boldsymbol{k})$ gives

$$\begin{aligned}\Omega_n^z(\boldsymbol{k}) &= i\epsilon_{xy}\left[\boldsymbol{\sigma}_3\frac{\partial T^\dagger(\boldsymbol{k})}{\partial k_x}\boldsymbol{\sigma}_3\frac{\partial T(\boldsymbol{k})}{\partial k_y}\right]_{nn} = i\epsilon_{xy}\left\{\boldsymbol{\sigma}_3\frac{\partial\left[T^{\dagger *}(\boldsymbol{k})C^{\dagger *}\right]}{\partial k_x}\boldsymbol{\sigma}_3\frac{\partial\left[C^*T^*(\boldsymbol{k})\right]}{\partial k_y}\right\}_{nn} = i\epsilon_{xy}\left[\boldsymbol{\sigma}_3\frac{\partial T^{\dagger *}(\boldsymbol{k})}{\partial k_x}C^{\dagger *}\boldsymbol{\sigma}_3 C^*\frac{\partial T^*(\boldsymbol{k})}{\partial k_y}\right]_{nn} \\ &= i\epsilon_{xy}\left[\boldsymbol{\sigma}_3\frac{\partial T^{\dagger *}(\boldsymbol{k})}{\partial k_x}\boldsymbol{\sigma}_3\frac{\partial T^*(\boldsymbol{k})}{\partial k_y}\right]_{nn} = -i\epsilon_{xy}\left[\boldsymbol{\sigma}_3\frac{\partial T^\dagger}{\partial k_x}\boldsymbol{\sigma}_3\frac{\partial T}{\partial k_y}\right]_{nn} = -\Omega_n^z(\boldsymbol{k}),\end{aligned} \tag{S85}$$

where we have used $\boldsymbol{\sigma}_3 = \boldsymbol{\sigma}_3^* = \left(\mathcal{C}^\dagger\boldsymbol{\sigma}_3\mathcal{C}\right)^* = \mathcal{C}^*\boldsymbol{\sigma}_3^*\mathcal{C}^{\dagger *} = \mathcal{C}^*\boldsymbol{\sigma}_3\mathcal{C}^{\dagger *}$ together with noticing that $\mathcal{C}$ does not depend on the wave vector $\boldsymbol{k}$. Equation (S85) implies that the Berry curvature must be zero. In other words, broken $\mathcal{PT}$ symmetry is a *necessary* requirement for *non-zero* Berry curvature in the magnon-phonon system.

2. *Effective time-reversal symmetry*

Even when the Berry curvature is non-zero locally in the k-space, the thermal Hall conductivity will vanish when the sum of the Berry curvature over the BZ is zero. Specifically, when the system is invariant under the effective time reversal symmetry, i.e., when the BdG Hamiltonian satisfies

$$\Theta H(\boldsymbol{k})\Theta^{-1} = H(-\boldsymbol{k}). \tag{S86}$$

Here Θ is the antiunitary time-reversal operator satisfying $\Theta^2 = +1$, which can be written as $\Theta = \mathcal{D}^\dagger\mathcal{K}$ where $\mathcal{D}$ is a paraunitary matrix obeying $\mathcal{D}^\dagger\boldsymbol{\sigma}_3\mathcal{D} = \mathcal{D}\boldsymbol{\sigma}_3\mathcal{D}^\dagger = \boldsymbol{\sigma}_3$ and $\mathcal{K}$ is the complex conjugate operator. The BdG Hamiltonian then obeys

$$\mathcal{D}^\dagger H^*(\boldsymbol{k})\mathcal{D} = H(-\boldsymbol{k}). \tag{S87}$$

By rewriting Eq. (S28) as

$$\boldsymbol{\sigma}_3 H(-\boldsymbol{k})T(-\boldsymbol{k}) = T(-\boldsymbol{k})\boldsymbol{\sigma}_3 E(-\boldsymbol{k}) \tag{S88}$$

and by inserting Eq. (S87) into Eq. (S88), we obtain

$$\boldsymbol{\sigma}_3\mathcal{D}^\dagger H^*(\boldsymbol{k})\mathcal{D}T(-\boldsymbol{k}) = T(-\boldsymbol{k})\boldsymbol{\sigma}_3 E(-\boldsymbol{k}). \tag{S89}$$

Multiplying both sides of Eq. (S89) by $\mathcal{D}$ from the left

$$\mathcal{D}\boldsymbol{\sigma}_3\mathcal{D}^\dagger H^*(\boldsymbol{k})\mathcal{D}T(-\boldsymbol{k}) = \mathcal{D}T(-\boldsymbol{k})\boldsymbol{\sigma}_3 E(-\boldsymbol{k}), \tag{S90}$$

leads to

$$\boldsymbol{\sigma}_3 H^*(\boldsymbol{k})\mathcal{D}T(-\boldsymbol{k}) = \mathcal{D}T(-\boldsymbol{k})\boldsymbol{\sigma}_3 E(-\boldsymbol{k}). \tag{S91}$$

Taking complex conjugate of both sides of Eq. (S91) yields

$$\left[\boldsymbol{\sigma}_3 H^*(\boldsymbol{k})\mathcal{D}T(-\boldsymbol{k})\right]^* = \left[\mathcal{D}T(-\boldsymbol{k})\boldsymbol{\sigma}_3 E(-\boldsymbol{k})\right]^*, \tag{S92}$$

so, that finally we obtain

$$\boldsymbol{\sigma}_3 H(\boldsymbol{k})\mathcal{D}^* T^*(-\boldsymbol{k}) = \mathcal{D}^* T^*(-\boldsymbol{k})\boldsymbol{\sigma}_3 E(-\boldsymbol{k}). \tag{S93}$$

Note that the effective time reversal symmetry also imposes $E(-\boldsymbol{k}) = E(\boldsymbol{k})$, so that

$$\boldsymbol{\sigma}_3 H(\boldsymbol{k})\mathcal{D}^* T^*(-\boldsymbol{k}) = \mathcal{D}^* T^*(-\boldsymbol{k})\boldsymbol{\sigma}_3 E(\boldsymbol{k}). \tag{S94}$$

In the same manner as $\mathcal{PT}$ symmetry, this leads to $T(\boldsymbol{k}) = \mathcal{D}^* T^*(-\boldsymbol{k})$. One can easily show that because of this condition the Berry curvature must satisfy

$$\Omega^z_n(\boldsymbol{k}) = -\Omega^z_n(-\boldsymbol{k}), \tag{S95}$$

which leads to a zero thermal Hall conductivity when we integrate (or sum) the Berry curvature over the entire BZ. Applying this result to the case of 2D AFM $FePS_3$ at zero magnetic field ($B_z = 0$), under which condition the magnon-phonon system is invariant under the effective time-reversal symmetry $\Theta = \mathcal{T}' = \mathcal{TC}$, leads to zero thermal Hall conductivity κ_{xy}, as discussed in relation to Eq. (9) in the main text.

C. Spin Berry curvature

The out-of-plane spin Berry curvature, involving S^z operator of electron spin, is given by

$$\begin{aligned}
\Omega^z_{S^z,n} &= \sum_{m\neq n} i\hbar^2 \sigma_3^{nn}\sigma_3^{mm} \frac{\langle n(\boldsymbol{k})|j_x^{S^z}|m(\boldsymbol{k})\rangle\langle m(\boldsymbol{k})|v_y|n(\boldsymbol{k})\rangle}{\left[\sigma_3^{nn}E_n(\boldsymbol{k}) - \sigma_3^{mm}E_m(\boldsymbol{k})\right]^2} - (k_x \longleftrightarrow k_y) \\
&= -2\hbar^2 \sum_{m\neq n} \sigma_3^{nn}\sigma_3^{mm} \mathrm{Im}\left\{\frac{\langle n(\boldsymbol{k})|j_x^{S^z}|m(\boldsymbol{k})\rangle\langle m(\boldsymbol{k})|v_y|n(\boldsymbol{k})\rangle}{\left[\sigma_3^{nn}E_n(\boldsymbol{k}) - \sigma_3^{mm}E_m(\boldsymbol{k})\right]^2}\right\} \\
&= -2\hbar^2 \sum_{m\neq n} \sigma_3^{nn}\sigma_3^{mm} \mathrm{Im}\left\{\frac{\langle n(\boldsymbol{k})|S^z\boldsymbol{\sigma}_3 v_x + v_x\boldsymbol{\sigma}_3 S^z|m(\boldsymbol{k})\rangle\langle m(\boldsymbol{k})|v_y|n(\boldsymbol{k})\rangle}{\left[\sigma_3^{nn}E_n(\boldsymbol{k}) - \sigma_3^{mm}E_m(\boldsymbol{k})\right]^2}\right\}.
\end{aligned} \tag{S96}$$

Here Im denotes the imaginary part of a complex number. Using the completeness Eq. (S62), and noting that $\boldsymbol{\sigma}_3\boldsymbol{\sigma}_3 = \mathcal{I}$, we obtain

$$\begin{aligned}
&\langle n(\boldsymbol{k})|S^z\boldsymbol{\sigma}_3 v_x + v_x\boldsymbol{\sigma}_3 S^z|m(\boldsymbol{k})\rangle = \langle n(\boldsymbol{k})|S^z\boldsymbol{\sigma}_3 v_x|m(\boldsymbol{k})\rangle + \langle n(\boldsymbol{k})|v_x\boldsymbol{\sigma}_3 S^z|m(\boldsymbol{k})\rangle \\
&= \langle n(\boldsymbol{k})|S^z\sum_l \sigma_3^{ll}|l(\boldsymbol{k})\rangle\langle l(\boldsymbol{k})|\boldsymbol{\sigma}_3\boldsymbol{\sigma}_3 v_x|m(\boldsymbol{k})\rangle + \langle n(\boldsymbol{k})|v_x\sum_q \sigma_3^{qq}|q(\boldsymbol{k})\rangle\langle q(\boldsymbol{k})|\boldsymbol{\sigma}_3\boldsymbol{\sigma}_3 S^z|m(\boldsymbol{k})\rangle \\
&= \langle n(\boldsymbol{k})|S^z\sum_l \sigma_3^{ll}|l(\boldsymbol{k})\rangle\langle l(\boldsymbol{k})|v_x|m(\boldsymbol{k})\rangle + \langle n(\boldsymbol{k})|v_x\sum_q \sigma_3^{qq}|q(\boldsymbol{k})\rangle\langle q(\boldsymbol{k})|S^z|m(\boldsymbol{k})\rangle,
\end{aligned} \tag{S97}$$

and, therefore,

$$\begin{aligned}
&\langle n(\boldsymbol{k})|S^z\boldsymbol{\sigma}_3 v_x + v_x\boldsymbol{\sigma}_3 S^z|m(\boldsymbol{k})\rangle = \langle n(\boldsymbol{k})|S^z\sigma_3^{nn}|n(\boldsymbol{k})\rangle\langle n(\boldsymbol{k})|v_x|m(\boldsymbol{k})\rangle + \langle n(\boldsymbol{k})|v_x\sigma_3^{mm}|m(\boldsymbol{k})\rangle\langle m(\boldsymbol{k})|S^z|m(\boldsymbol{k})\rangle \\
&+ \sum_{l\neq n}\langle n(\boldsymbol{k})|S^z\sigma_3^{ll}|l(\boldsymbol{k})\rangle\langle l(\boldsymbol{k})|v_x|m(\boldsymbol{k})\rangle + \sum_{q\neq m}\langle n(\boldsymbol{k})|v_x\sigma_3^{qq}|q(\boldsymbol{k})\rangle\langle q(\boldsymbol{k})|S^z|m(\boldsymbol{k})\rangle \\
&= \left(\sigma_3^{nn}S^z_{nn} + \sigma_3^{mm}S^z_{mm}\right)\langle n(\boldsymbol{k})|v_x|m(\boldsymbol{k})\rangle + \sum_{l\neq n}\sigma_3^{ll}S^{z,\boldsymbol{k}}_{nl}\langle l(\boldsymbol{k})|v_x|m(\boldsymbol{k})\rangle + \sum_{q\neq m}\sigma_3^{qq}S^{z,\boldsymbol{k}}_{qm}\langle n(\boldsymbol{k})|v_x|q(\boldsymbol{k})\rangle.
\end{aligned} \tag{S98}$$

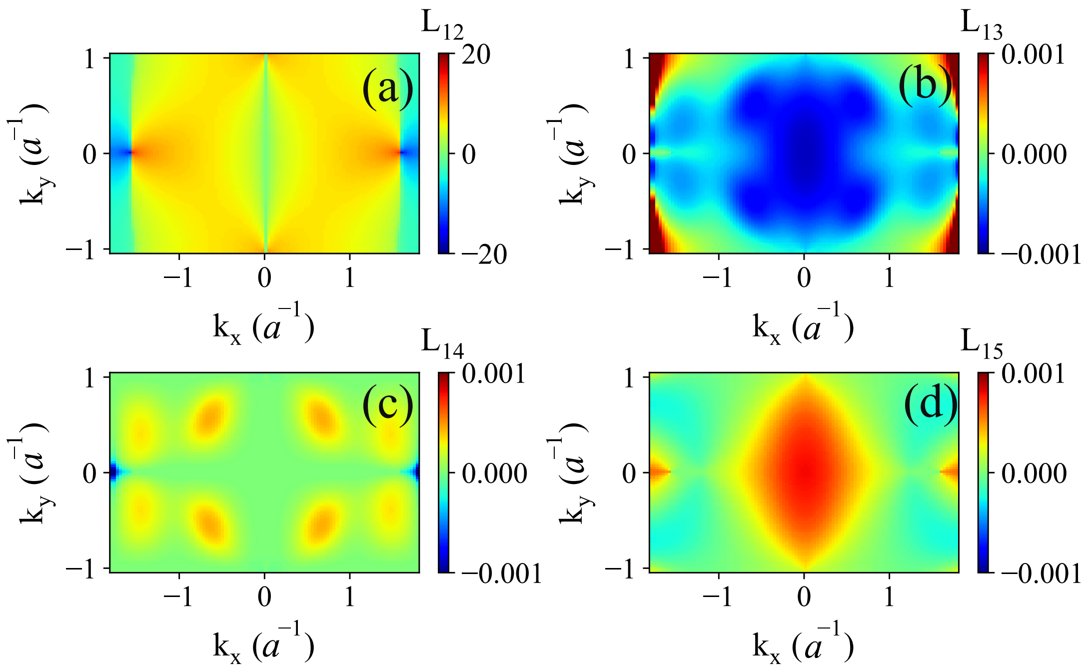

Figure S6. The *projected* spin Berry curvature $\Omega^z_{S^z,nm}$ [Eq. (S103)] of magnon-phonon bands in 2D AFM $FePS_3$ as a function of the in-plane wave vector (k_x, k_y) within the first BZ calculated without applied magnetic field ($B_z = 0$ T). The color bar encodes the magnitude of the function $L_{ij} = \mathrm{sgn}(\Omega^z_{S^z,ij}) \log(1 + |\Omega^z_{S^z,ij}|)$.

By inserting Eq. (S98) into Eq. (S96), we can decompose the spin Berry curvature into two terms

$$\Omega^z_{S_z,n} = \Omega^{z,(1)}_{S^z,n} + \Omega^{z,(2)}_{S^z,n}, \tag{S99}$$

where

$$\begin{aligned}\Omega^{z,(1)}_{S^z,n} &= -2\hbar^2 \sum_{m\neq n} \left(\sigma_3^{nn} S^z_{nn} + \sigma_3^{mm} S^z_{mm}\right) \sigma_3^{nn}\sigma_3^{mm} \mathrm{Im}\left\{\frac{\langle n(\boldsymbol{k})|v_x|m(\boldsymbol{k})\rangle\langle m(\boldsymbol{k})|v_y|n(\boldsymbol{k})\rangle}{\left[\sigma_3^{nn}E_n(\boldsymbol{k}) - \sigma_3^{mm}E_m(\boldsymbol{k})\right]^2}\right\} \\ &= \sum_{m\neq n} \left(\sigma_3^{nn} S^z_{nn} + \sigma_3^{mm} S^z_{mm}\right) \Omega^z_{nm}(\boldsymbol{k}),\end{aligned} \tag{S100}$$

and

$$\Omega^{z,(2)}_{S^z,n} = -2\hbar^2 \sum_{m\neq n} \sigma_3^{nn}\sigma_3^{mm} Im\left\{\sum_{l\neq n} \sigma_3^{ll} S^{z,\boldsymbol{k}}_{nl} \frac{\langle l(\boldsymbol{k})|v_x|m(\boldsymbol{k})\rangle\langle m(\boldsymbol{k})|v_y|n(\boldsymbol{k})\rangle}{\left[\sigma_3^{nn}E_n(\boldsymbol{k}) - \sigma_3^{mm}E_m(\boldsymbol{k})\right]^2} + \sum_{q\neq m} \sigma_3^{qq} S^{z,\boldsymbol{k}}_{qm} \frac{\langle m(\boldsymbol{k})|v_y|n(\boldsymbol{k})\rangle\langle n(\boldsymbol{k})|v_x|q(\boldsymbol{k})\rangle}{\left[\sigma_3^{nn}E_n(\boldsymbol{k}) - \sigma_3^{mm}E_m(\boldsymbol{k})\right]^2}\right\}. \tag{S101}$$

Here $S^z_{ii} = \langle i(\boldsymbol{k})|S^z|i(\boldsymbol{k})\rangle$ is the diagonal spin expectation value of the ith band and $S^{z,\boldsymbol{k}}_{ij} = \langle i(\boldsymbol{k})|S^z|j(\boldsymbol{k})\rangle$ is the off-diagonal spin expectation value; and $\Omega^z_{nm}(\boldsymbol{k})$ is the projected Berry curvature of the nth band on the mth band given by

$$\Omega^z_{nm}(\boldsymbol{k}) = -2\hbar^2 \mathrm{Im}\left\{\frac{\langle n(\boldsymbol{k})|v_x|m(\boldsymbol{k})\rangle\langle m(\boldsymbol{k})|v_y|n(\boldsymbol{k})\rangle}{\left[\sigma_3^{nn}E_n(\boldsymbol{k}) - \sigma_3^{mm}E_m(\boldsymbol{k})\right]^2}\right\}, \tag{S102}$$

We define the *projected* spin Berry curvature as

$$\Omega^z_{S^z,nm} = -2\hbar^2 \sigma_3^{nn}\sigma_3^{mm} \mathrm{Im}\left\{\frac{\langle n(\boldsymbol{k})|S^z\boldsymbol{\sigma}_3 v_x + v_x\boldsymbol{\sigma}_3 S^z|m(\boldsymbol{k})\rangle\langle m(\boldsymbol{k})|v_y|n(\boldsymbol{k})\rangle}{\left[\sigma_3^{nn}E_n(\boldsymbol{k}) - \sigma_3^{mm}E_m(\boldsymbol{k})\right]^2}\right\}. \tag{S103}$$

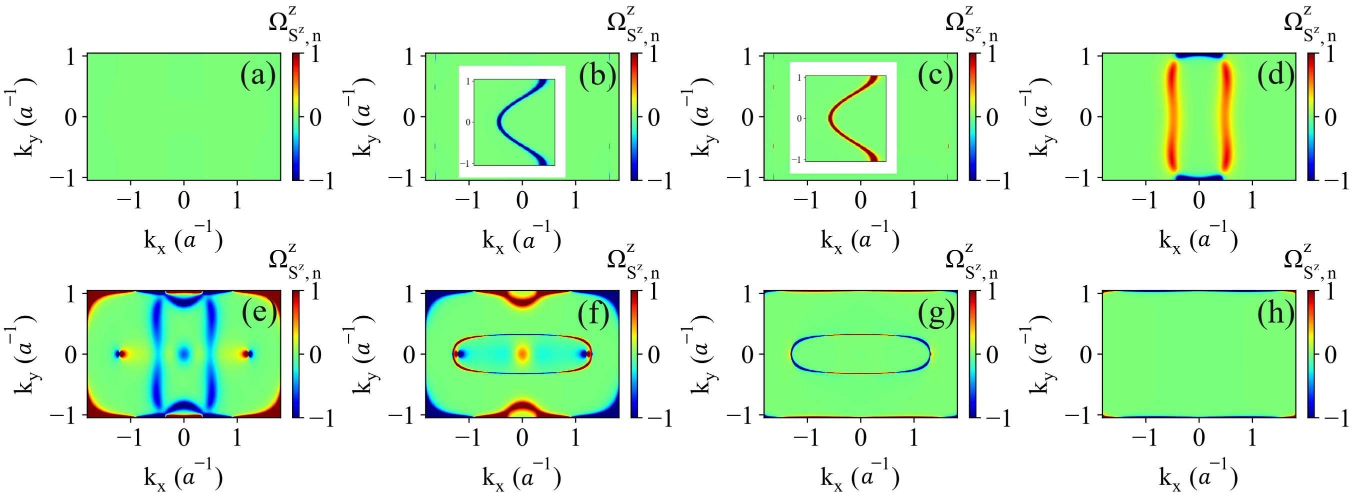

Figure S7. The spin Berry curvature of magnon-phonon band in 2D AFM $FePS_3$ as a function of the in-plane wave vector (k_x, k_y) within the first BZ calculated with an applied magnetic field $B_z = 30$ T for (a)–(h) 1st–8th band [Fig. S2], respectively. The color bar encodes the magnitude of the spin Berry curvature $\Omega^z_{S^z,n}$ of the nth band. The insets in panels (b) and (c) show a zoom in around $k_x = -1.64\ a^{-1}$ where the spin Berry curvature of the corresponding bands is non-zero.

The first contribution, $\Omega^{z,(1)}_{S^z,n}$, to the spin Berry curvature reveals a relationship between the topological transverse transport of spin with the Berry curvature and, therefore, the non-zero Chern number induced by magnon-phonon hybridization. Conversely, the second contribution, $\Omega^{z,(2)}_{S^z,n}$, describes the spin Nernst conductivity occurring due to the spin coupling between different magnon and phonon bands, and it is not related to the Chern number.

At zero applied magnetic field, $(\sigma_3^{nn} S^z_{nn} + \sigma_3^{mm} S^z_{mm})$ does not depend on the wave vector $\boldsymbol{k}$, so the spin Nernst conductivity originating from the first term $[\Omega^{z,(1)}_{S^z,n}]$ vanishes when we take the sum or integral of $\Omega^{z,(1)}_{S^z,n}$ over the entire BZ. The spin Nernst conductivity then depends only on the second term, $\Omega^{z,(2)}_{S^z,n}$, which can reach large magnitude via interband transitions between magnon-like bands mediated by the coupling to phonons. There are also smaller contributions from magnon-mediated interband transitions between phonon-like bands, as discussed in the main text. Figure S6 shows the projected spin Berry curvature $\Omega^z_{S^z,nm}$ calculated from Eq. (S103) for the 1st band acting on the 2nd, 3rd, 4th (magnon-like) and 5th (phonon-like) band. The phonon-mediated interband transitions between the two magnon-like bands having opposite helicity dominates the spin Berry curvature of the 1st band—this is made clear by comparing the magnitude of the projected spin Berry curvature $\Omega^z_{S^z,12}$ with the total spin Berry curvature $\Omega^z_{S^z,1}$ [Fig. 5(a) in the main text]. In contrast, the 3rd, 4th and 5th bands shown in Fig. S5 provide minor contributions to the spin Berry curvature of the 1st (magnon-like) band.

When a finite magnetic field is applied perpendicular to the system, the second term $\Omega^{z,(2)}_{S^z,n}$, accounting for interband transitions between magnon-like bands mediated by phonons, decays quickly because the gap between two magnon bands possessing opposite spin polarization increases. In contrast, the second contribution $\Omega^{z,(2)}_{S^z,n}$, which accounts for interband transitions between phonon-like bands mediated by magnons, remains unaffected by the applied magnetic field. This is because the energy separation between the two phonon bands remains constant. Consequently, in this region the spin Nersnt conductivity is mainly governed by the Chern number originating from $\Omega^{z,(1)}_{S^z,n}$ contribution as well as the interband transitions between phonon bands in the second contribution $\Omega^{z,(2)}_{S^z,n}$ mediated by magnons. To illustrate this, Fig. S7 shows the spin Berry curvature of the magnon-phonon bands in the presence of an applied magnetic field of $B_z =$ 30 T. One can observe the contributions of the Chern number to the spin Nernst conductivity in this figure through the shape of the spin Berry curvatures of the 1st to 4th magnon bands that is similar to that of the Berry curvatures in Fig. 4(a)–(d) in the main text. The other phonon bands have mixed contributions from the Chern number and magnon-mediated interband transitions between phonon-like bands.

D. Handling Berry curvature and spin Berry curvature in a system with exceptional points

We note that both Berry and spin Berry curvatures are not well-defined at band touching points, known as exceptional points (EPs), in the dispersion of a bosonic system. In 2D AFM $FePS_3$, EPs occur at the X and M points in the magnon-phonon band structure [Fig. 2(a) in the main text]. To avoid divergence of the Berry and spin Berry curvatures at the EPs and calculate the Chern number, we adopt the technique proposed in Ref. [17]. This technique involves extending to a complex k-space by introducing an imaginary component of the momentum [17]. Using this approach, we can calculate the Chern number for a specific band in our system without encountering singularities. Alternatively, we can introduce a small energy gap at the EPs by adding $\Delta E \approx 10^{-4}$ meV to the denominator of the expressions for the Berry and spin Berry curvatures [Eqs. (14) and (15) in the main text]. Either way, we find that the contribution from EPs to the Chern number is negligible, apart from causing the Berry and spin Berry curvatures to diverge at specific points in the standard k-space composed of real $\boldsymbol{k}$ vectors.

---

[1] T. Holstein and H. Primakoff, Field dependence of the intrinsic domain magnetization of a ferromagnet, Phys. Rev. **58**, 1098 (1940).

[2] U. Bajpai, A. Suresh, and B. K. Nikolić, Quantum many-body states and Green's functions of nonequilibrium electron-magnon systems: Localized spin operators versus their mapping to Holstein-Primakoff bosons, Phys. Rev. B **104**, 184425 (2021).

[3] S. Park, N. Nagaosa, and B.-J. Yang, Thermal Hall effect, spin Nernst effect, and spin density induced by a thermal gradient in collinear ferrimagnets from magnon-phonon interaction, Nano Lett. **20**, 2741 (2020).

[4] R. Matsumoto, R. Shindou, and S. Murakami, Thermal Hall effect of magnons in magnets with dipolar interaction, Phys. Rev. B **89**, 054420 (2014).

[5] J. H. P. Colpa, Diagonalization of the quadratic boson Hamiltonian, Phys. A: Stat. Mech. Appl. **93**, 327 (1978).

[6] R. M. White, M. Sparks, and I. Ortenburger, Diagonalization of the antiferromagnetic magnon-phonon interaction, Phys. Rev. **139**, A450 (1965).

[7] M. Amirabbasi and P. Kratzer, Orbital and magnetic ordering in single-layer $FePS_3$: A DFT+U study, Phys. Rev. B **107**, 024401 (2023).

[8] S. Liu, A. Granados del Águila, D. Bhowmick, C. K. Gan, T. Thu Ha Do, M. A. Prosnikov, D. Sedmidubský, Z. Sofer, P. C. M. Christianen, P. Sengupta, and Q. Xiong, Direct observation of magnon-phonon strong coupling in two-dimensional antiferromagnet at high magnetic fields, Phys. Rev. Lett. **127**, 097401 (2021).

[9] P.-O. Löwdin, A note on the quantum-mechanical perturbation theory, J. Chem. Phys. **19**, 1396 (1951).

[10] P.-O. Löwdin, Partitioning technique, perturbation theory, and rational approximations, Int. J. Quantum Chem. **21**, 69 (1982).

[11] L. Jin and Z. Song, Partitioning technique for discrete quantum systems, Phys. Rev. A **83**, 062118 (2011).

[12] J. R. Schrieffer and P. A. Wolff, Relation between the Anderson and Kondo Hamiltonians, Phys. Rev. **149**, 491 (1966).

[13] S. Bravyi, D. P. DiVincenzo, and D. Loss, Schrieffer-Wolff transformation for quantum many-body systems, Ann. Phys. **326**, 2793 (2011).

[14] Z. Zhou, L.-L. Wan, and Z.-F. Xu, Topological classification of excitations in quadratic bosonic systems, J. Phys. A: Math. Theor. **53**, 425203 (2020).

[15] L.-L. Wan, Z. Zhou, and Z.-F. Xu, Squeezing-induced topological gap opening on bosonic Bogoliubov excitations, Phys. Rev. A **103**, 013308 (2021).

[16] G. Massarelli, I. Khait, and A. Paramekanti, Krein-unitary Schrieffer-Wolff transformation and band touchings in bosonic Bogoliubov-de Gennes and other Krein-Hermitian Hamiltonians, Phys. Rev. B **106**, 144434 (2022).

[17] T. Ohashi, S. Kobayashi, and Y. Kawaguchi, Generalized Berry phase for a bosonic Bogoliubov system with exceptional points, Phys. Rev. A **101**, 013625 (2020).